International Journal of Thermal Sciences 220 (2026) 110319

Contents lists available at ScienceDirect

International Journal of Thermal Sciences

journal homepage: www.elsevier.com/locate/ijts

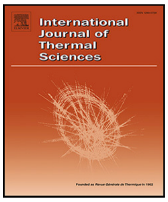

An optimization study considering MNP temporal evolution improves therapeutic efficacy in hyperthermia treatment

Buchen Wu [a,1], Qian Jiang [b,*,1], Zhaokun Wang [b], Chenglei Wang [c], Feng Ren [d], Hui Tang [b]

[a] Department of Mechanical and Aerospace Engineering, The Hong Kong University of Science and Technology, Clear Water Bay, Hong Kong, China
[b] Department of Mechanical Engineering, The Hong Kong Polytechnic University, Hong Kong, China
[c] Institute of High Performance Computing (IHPC), Agency for Science, Technology and Research (A*STAR), 1 Fusionopolis Way, #16-16 Connexis, 138632, Singapore
[d] School of Marine Science and Technology, Northwestern Polytechnical University, Xi'an, Shaanxi, China

ARTICLE INFO

Keywords:
Bioheat transfer
Heat and mass transfer
Thermal dose
Magnetic hyperthermia
Optimization

ABSTRACT

This work investigates optimal strategies for achieving the most effective tumor ablation outcomes in magnetic hyperthermia by incorporating the thermal exposure time, magnetic nanoparticle (MNP) dose, injection sites, and waiting time before alternating magnetic field (AMF) application. The optimization framework highlights the significance of thermal exposure time, as this treatment duration substantially influences the temporary distribution of the heat source, i.e., MNPs, and consequently affects the thermal dose for efficacy evaluation. Multi-site MNP injections are involved in both circular and elliptical tumor configurations, and a transversal blood vessel introduces asymmetric cooling effects. This optimization framework can achieve efficient convergence, demonstrating its effectiveness in identifying the optimal strategy. Without the influence of the blood vessel, optimal injections exhibit a centrosymmetric distribution in the circular tumor model; comparatively, a linear distribution along the major axis with approximately halved treatment duration is observed in the elliptical model. When the blood vessel is nearby, the notable asymmetric cooling effects complicate treatment, where the random search method is more effective. Increasing the tumor–vessel distance enhances tumor ablation, reduces MNP dosage and treatment time, and decreases the average injection site deviation; however, the impact becomes marginal at larger distances. This optimization study facilitates the efficacy of practical treatment.

1. Introduction

Magnetic hyperthermia, also named magnetic thermal therapy, is a cancer ablation approach developed in recent decades [1]. When exposed to the high-frequency alternating magnetic field (AMF), the injected magnetic nanoparticles (MNPs) serve as the heat source during the treatment. By this mean, the heat diffused from the MNP causes the temperature of the tumor region to be elevated to approximately 42 to 46 °C, thereby leading to protein denaturation and ablation of the tumorous cells [2–7]. Compared with conventional therapies, magnetic hyperthermia has some advantages, such as precise and uniform heating, safety for the human body, and enhanced efficacy [8–10]. Proper utilization of magnetic hyperthermia can achieve optimal treatment outcomes, i.e., complete tumor tissue ablation while preserving surrounding healthy tissue. However, achieving the desired thermal dose for the tumor treatment poses challenges in magnetic hyperthermia, where precise management of intratumoral heat release from MNPs is critically important [11].

Practically, hysteresis and relaxational losses are key mechanisms for heat generation when MNPs are subjected to an external AMF [12]. However, the MNPs employed in magnetic hyperthermia are typically small enough to be deemed superparamagnetic nanoparticles, indicating that only the relaxation losses contribute to the thermal effect [13–15]. Rosensweig [16] proposed an analytical formulation for calculating the heat generated by MNPs when exposed to AMF. This widely adopted method offers an accurate approach to quantify heat generation during magnetic hyperthermia treatment, and highlights the significance of the distribution of MNPs in determining the heating pattern [13,17–20].

Previous studies indicate that a more spread-out distribution of MNPs facilitates a milder heating pattern in the intratumoral area, like a uniform spread or a Gaussian shape with a broader variance [11,21].

---

[*] Corresponding author.
E-mail address: qian2020.jiang@connect.polyu.hk (Q. Jiang).
[1] These authors contributed equally to this work.

https://doi.org/10.1016/j.ijthermalsci.2025.110319
Received 12 July 2025; Received in revised form 13 September 2025; Accepted 14 September 2025

Nomenclature

Abbreviations

AMF	Alternating magnetic field
CDE	Convection–diffusion equation
LBM	Lattice Boltzmann method
MNP	Magnetic nanoparticle
PBHTE	Pennes bio-beat transfer equation
PSO	Particle swarm optimization

Greek Letters

α	Thermal diffusivity, m^2/s
β	Inclined angle, °
β_0	Reference inclined angle, °
χ_0	Equilibrium susceptibility
δt	Time interval, s
δ	Distance between vessel and tumor, mm
μ_0	Vacuum permeability, Tm/A
ν	Kinematic viscosity, m^2/s
$\omega_1 \sim \omega_4$	Weighting coefficients
$\boldsymbol{\Phi}$	Volume fraction during waiting period
ϕ	Volume fraction during treatment
ϕ_0	Reference volume fraction
ρ	Density, kg/m^3
σ	Standard deviation, mm
σ_0	Reference standard deviation, mm
τ_R	Effective relaxation time, s

Roman Letters

$(\bar{x}, \bar{y})$	Average Cartesian coordinate, mm
(k_x, k_y)	Coordinate ratio
(x, y)	Cartesian coordinate, mm
(x_0, y_0)	Reference Cartesian coordinate, mm
$\boldsymbol{u}$	Velocity, m/s
$\dot{m}$	Mass flow rate, kg/m^3-s
c_p	Specific heat capacity, J/(kg-K)
C_{EM}	Coefficient for $CEM43$, a function of temperature
$CEM43$	Cumulative equivalent minutes at 43 °C, min
D	Mass diffusivity, m^2/s
d	Distance of injection site, mm
d_0	Reference distance, mm
f	Frequency of the AMF, Hz
H_0	Strength of the AMF, A/m
J	Objection function
k	Thermal conductivity, W/m-K
k_β	Inclined angle ratio
k_ϕ	Volume fraction ratio
k_σ	Standard deviation ratio
k_d	Distance ratio of injection site
L	Length of healthy tissue, mm
l	Number of time steps
n	Injection number
p	Pressure, Pa
Q	Heat source density from MNP, W/m^3
R_{CEM43}	Requirement for ablation ratio
R_{dose}	Requirement for MNP dose
R_{Tarea}	Requirement for safe temperature
R_{Tmax}	Requirement for maximum temperature
S	Area, mm^2
T	Temperature, °C
t_t	treatment time, min
t_w	Waiting time before AMF application, min
V	Volume of injected MNP solution, m^2
w	Width of blood vessel, mm

Subscripts

b	Blood
h	Horizontal
i	Injection number index
max	Maximum value
nf	Nanofluid, the mixture of tissue and injected MNPs
opt	Optimal value
$tumor$	Tumor tissue
v	Vertical

The Gaussian distribution is widely regarded as the theoretical pattern resulting from the injection of MNPs at a single site [22]. In contrast, multi-site injections typically generate a more uniform temperature distribution, effectively covering a larger area than single-site injections. Such an injection approach reduces the risk of overheating and enhances therapeutic efficacy [23–26].

Several optimization studies have been conducted to identify the optimal distribution of the heat source to enhance the efficacy of magnetic hyperthermia treatment. These studies often incorporate optimization techniques with the widely used Pennes bio-heat transfer equation (PBHTE) [27]. Among them, most investigations rely on local optimization algorithms, which are limited by their dependence on initial assumptions [28–30]. Due to constraints in the optimization algorithms and their configurations, the treatment outcomes reported in these studies are often suboptimal. Specifically, achieving complete ablation of the tumor tissue while preserving surrounding healthy tissue remains a significant challenge. However, existing studies utilizing global optimization techniques on this topic frequently fail to meet critical temperature requirements due to arrangements that are not entirely reasonable, leading to considerable damage to healthy tissues [31,32]. Jiang et al. [25] utilized particle swarm optimization (PSO) to determine the optimal heat source distribution, successfully achieving an ideal temperature profile. However, the evolution of MNPs during treatment, which changes with thermal exposure time and subsequently affects the heat generation pattern, has not been investigated; instead, the efficacy is assessed based on the stationary temperature in this study. Thus far, to the best of the authors' knowledge, the investigations about optimizing the effective tumor ablation in magnetic hyperthermia, considering the impact of treatment duration on MNP mass transfer and thermal dose, remain sparse, despite the significant effects observed [33–37].

Therefore, to address this research gap and facilitate tumor ablation, the present work employs the PSO algorithm to identify the minimum amount of MNP required for optimal efficacy, accounting for the impact of treatment duration on MNP temporary distribution and thermal dose in tumor ablation. The temperature field and MNP distribution are governed by the PBHTE and the concentration equation, respectively, while the optimal efficacy is selected using the PSO algorithm. Circular and elliptical tumor models are utilized, involving both single-site and multi-site MNP injections. The objectives of this work are: (i) treatment duration is incorporated in the objective function to facilitate the optimal treatment strategies; (ii) ablation strategies are identified and enhanced for the complex scenario involving a transverse vessel, with the consideration of its significant cooling effect [38–40]; (iii) the impact of tumor–vessel distance is examined, with a discussion of the commonalities and variations among the optimal strategies. Consequently, the remainder of the paper is organized as follows: Section 2 details the problem description and methodology, introducing the schematics, numerical approach, and optimization model. Section 3 presents results categorized by the impact of the blood vessel. Section 3.1 focuses on scenarios where the tumor is distant from the vessel, examining optimal efficacy in both circular and elliptical tumor models. Subsequently, Section 3.2 incorporates the nearby vessel flow into the simulation, quantifying the cooling effects and refining the ablation strategy to enhance efficacy across various tumor–vessel distances. The conclusive findings are summarized in Section 4.

2. Problem description and methodology

This section introduces the physical and numerical models employed in this study. In Section 2.1, two selected tumor models and their physical configurations are presented. Subsequently, the governing equations for the magnetic hyperthermia treatment are introduced in Section 2.2. In Section 2.3, the thermal dose model for evaluating the treatment efficacy is described. Finally, the optimization algorithm is presented in Section 2.4.

2.1. Problem description

Magnetic hyperthermia involves complex heat and mass transfer processes in practice. In the present work, two tumor models are considered: a circular tumor model and an elliptical tumor model (see Fig. 1), representing geometric variations. The diameter of the circular tumor is set to 10 mm, a size commonly observed in medical cases [41]. To facilitate comparison and analysis, the elliptical tumor model is designed to have the same area as the circular tumor model, with the major and minor axes set to 12.5 mm and 8 mm, respectively. These two tumor models are placed centrally within a 50 mm × 50 mm block of healthy tissue. According to the previous study [25], the size of the computational domain is sufficiently large for this problem. A straight blood vessel traversing horizontally through the healthy tissue is located near the tumor, where the direction of blood flow is along the x-axis. The width of the straight blood vessel is set at $w = 5$ mm, and the distance δ between the vessel and the tumor is varied to investigate the significant asymmetric cooling effects induced by nearby blood flow. The vessel wall remains stationary, and the flow inside the vessel is assumed to be steady and fully developed. To minimize the overheating risk during the treatment, the heat source material (i.e., MNP) is designed to diffuse for a short period before exposure to the AMF (which is assumed to be spatially uniform in the horizontal direction). Consequently, the initial distribution of MNP results from the short-time MNP diffusion at the injection locations. The heating of the tumor tissue begins with the AMF application, and MNPs continue to diffuse. The outer boundary conditions for MNP concentration (represented by volume fraction) and temperature are specified as 0 and 37 °C, respectively, to reflect the normal conditions of the human body.

2.2. Governing equations

As presented above, the MNP volume fraction ϕ and temperature T are evaluated using a concentration equation [34] and an energy equation [27], respectively, during the treatment. The flow velocity $\mathbf{u}$ in the blood vessel is governed by the incompressible Navier–Stokes equations [42]. Hence, the governing equations of this two-dimensional system can be expressed as

$$\nabla \cdot \mathbf{u} = 0, \tag{1a}$$

$$\frac{\partial \mathbf{u}}{\partial t} + \mathbf{u} \cdot \nabla \mathbf{u} = -\frac{1}{\rho_b} \nabla p + \nu \nabla^2 \mathbf{u}, \tag{1b}$$

$$\frac{\partial T}{\partial t} + \mathbf{u} \cdot \nabla T = \alpha_{nf} \nabla^2 T + \frac{1}{(\rho c_p)_{nf}} \dot{m}_b c_{p,b} (T_b - T) + \phi \frac{Q}{(\rho c_p)_{nf}}, \tag{1c}$$

$$\frac{\partial \phi}{\partial t} + \mathbf{u} \cdot \nabla \phi = D \nabla^2 \phi, \tag{1d}$$

where p, ρ, c_p, and ν denote the pressure, density, specific heat capacity, and kinematic viscosity, respectively. $\alpha = k/(\rho c_p)$ is the thermal diffusivity, where k is the thermal conductivity. D is the MNP mass diffusivity. The subscript "nf" denotes properties of nanofluid or modified tissue, representing a mixture of the tissue or blood flow with the dispersed MNPs, while "b" denotes the properties of blood.

Eq. (1c) is actually a variant of PBHTE with an additional convection term, involving both the heat dissipation induced by blood perfusion $\dot{m}_b c_{p,b}(T_b - T)$ and the heat generation from the MNPs exposed to AMF ϕQ. Here, $T_b = 37$ °C represents the temperature of the perfusing blood, and $\dot{m}_b$ denotes the mass flow rate of blood. In practice, $\dot{m}_b$ is a temperature-dependent variable that differs between healthy tissue and tumor regions, as suggested by Lang et al. [43]. The heat source Q is obtained by Rosensweig's model [16]

$$Q = \pi \mu_0 \chi_0 H_0^2 f \frac{2\pi f \tau_R}{1 + (2\pi f \tau_R)^2}, \tag{2}$$

where μ_0, χ_0, H_0, f and τ_R are the vacuum permeability, the equilibrium susceptibility, the strength of the AMF, the frequency of AMF, and the effective relaxation time, respectively. Note that the effective relaxation time is determined by the Neel and Brownian relaxation times [12]. Further details can be found in our previous work [25].

The injected MNPs affect the thermal properties of the tissue and blood fluid through the local volume fraction ϕ, which is linearly related to χ_0 in Eq. (2) [16]. Iron-based nanoparticles, especially the magnetite (Fe_3O_4), have been widely utilized in magnetic hyperthermia treatment because of their low toxicity and excellent biocompatibility [44,45]. Therefore, Fe_3O_4 is selected as MNP in the present work. To simplify the computational process and enhance simulation efficiency, the thermal properties of healthy tissue, tumor tissue, and blood fluid are considered identical due to their minor discrepancies in practice [35,42,46]. The mixture of MNP and tissue/blood can be regarded as nanofluids [47–49], and the formulations for obtaining the thermal properties of nanofluids are illustrated in our previous work, along with the properties of each component of the mixture [25].

The analytical evolution of MNP concentration at ith injection site before the AMP application is determined by

$$\Phi_i(x, y, t_w) = \frac{V_i}{4\pi D t_w} \exp\left[-\frac{(x - x_i)^2 + (y - y_i)^2}{4 D t_w}\right], \tag{3}$$

where V_i denotes the volume of the ith injection. Eq. (3) indicates that, at any waiting time t_w, the initial volume fraction of the ith injected MNPs can be regarded as a Gaussian shape with a variance of $\sigma^2 = 2Dt_w$. Consequently, when AMF is applied, MNPs have diffused over a waiting time t_w, and the distribution of the ith injected MNPs can be rewritten as

$$\phi_i(x, y) = \frac{V_i}{2\pi\sigma^2} \exp\left[-\frac{(x - x_i)^2 + (y - y_i)^2}{2\sigma^2}\right]. \tag{4}$$

Given the very short waiting period for MNP diffusion before the application of AMF, we assume that the volume fraction of the initial MNPs follows linear superposition. Therefore, the initial MNP concentration at the beginning of treatment can be expressed as

$$\phi(x, y) = \sum_{i=1}^{n} \phi_i(x, y), \tag{5}$$

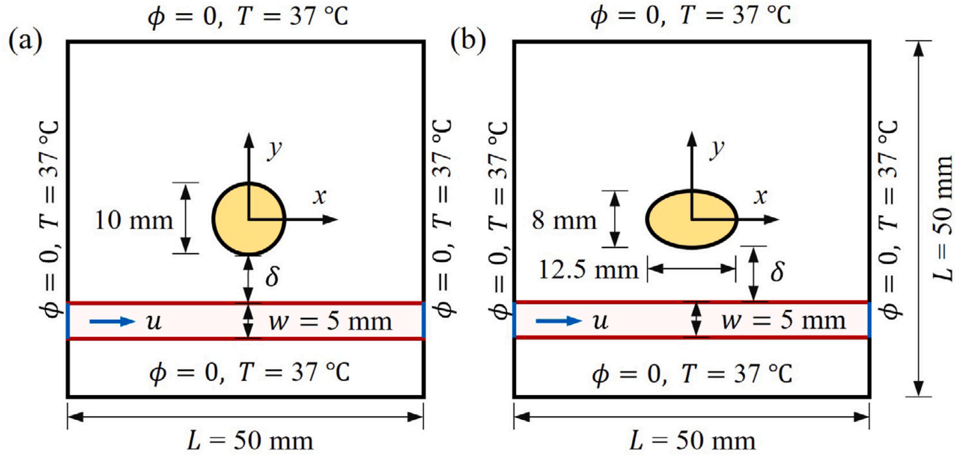

Fig. 1. Schematics of two tumor models embedded in healthy tissue: (a) a circular tumor model, and (b) an elliptical tumor model. The yellow regions denote the tumor tissue, the pink areas represent the vessel flow, and the white parts represent the healthy tissue.

where n denotes the total number of injections.

The governing equations (Eq. (1)) are solved by the multiple-relaxation-time lattice Boltzmann method (MRT-LBM) [50], where the fluid dynamics within the blood vessel are solved by the D2Q9 scheme, while the MNP concentration and temperature distributions are both calculated by the D2Q5 scheme. The validation of the numerical methods is detailed in Appendix.

2.3. Thermal dose

Cell ablation during magnetic hyperthermia results from the synergistic effects of thermal exposure time and temperature distribution [37,51]. This is particularly important when assessing cell death, as the temperature distribution is spatially non-uniform and temporally variable during treatment [52]. Therefore, a widely accepted $CEM43$ model [53,54] is adopted in this work to evaluate treatment efficacy, which quantifies the cumulative equivalent minutes at 43 °C as

$$CEM43 = \sum_{j=1}^{l} C_{EM}{}^{43-T_j}\,\delta t, \quad C_{EM} = \begin{cases} 0.25, & T_j \le 43\text{°C}, \\ 0.5, & T_j > 43\text{°C}, \end{cases} \tag{6}$$

where T_j is the average temperature at the jth time step. l denotes the total number of time steps and δt represents the time interval. Typically, tissue is regarded as ablated when the $CEM43$ exceeds 60 min [24,37].

2.4. Optimization

This study applies PSO, a global optimization method, for searching the optimal treatment strategy to achieve the best tumor ablation outcomes. According to the operational procedure mentioned in Section 2.1, the treatment strategy is governed by the following physical variables: the selection of injection sites for MNP (x_i, y_i), the waiting time t_{wi} before AMF application, the dosage V_i for the ith MNP injection, and treatment duration t_t for thermal exposure. The first four variables determine the MNP distribution at the beginning of treatment. To facilitate searching, these four variables at each injection are substituted by four parameters in the optimization process, including the two coordinates of injection location (x_i, y_i), the MNP volume fraction amplitude ϕ_i, and its corresponding variance σ_i^2 at the time when subjected to AMF.

To enhance efficient comparison, the injection parameters are normalized and represented by corresponding ratios. The spatial distribution of MNPs is evaluated using the standard deviation ratio $k_{\sigma,i} = \sigma_i/\sigma_0$, where σ_0 is a reference standard deviation obtained from the waiting time before AMF application. The initial MNP volume fraction amplitude is defined as $k_{\phi,i} = \phi_i/\phi_0$, with ϕ_0 being the reference volume fraction. Typically, the injection coordinates (x_i, y_i) are randomly distributed and searched using the ratio $(k_{x,i}, k_{y,i}) = (x_i/2x_0 + 0.5, y_i/2y_0 + 0.5)$, where (x_0, y_0) are the reference coordinates.

Specifically, for the symmetric problem where no vessel is involved, symmetric injection strategies are utilized in the scenarios with multi-site injections for simplification. Centrosymmetric injections are employed for circular tumors, while axisymmetric injections are used for elliptical tumors, following a similar approach as illustrated in our previous work, where the injection sites are determined based on the distance from the tumor center [25]. In symmetric cases with circular tumors, all injections share the same initial MNP distribution and the same distance d to the tumor center. On the other hand, in symmetric cases with elliptical tumors, the distance is separated into different directions: the horizontal distance d_h along the major axis, the vertical distance d_v along the minor axis, and the inclined distance d_β at an angle β. As such, the injection locations for these symmetric cases are obtained from the distance ratio $k_{d,i} = d_i/d_{0i}$, where d_{0i} represents the chosen reference distance and varies by direction. By combining the distance and its direction, injection sites (x_i, y_i) are determined. The parameters in the optimization framework are summarized in Table 1, and the schematic of the parameter search is presented in Fig. 2.

Therefore, the parameters of the ratios are typically constrained to the range of [0,1], leading to the transformation of Eq. (4) into

$$\begin{aligned} \phi_i(x, y) &= \frac{V_i}{2\pi\sigma^2} \exp\left[-\frac{(x - x_i)^2 + (y - y_i)^2}{2\sigma^2}\right] \\ &= k_{\phi,i}\phi_0 \exp\left\{-\frac{\left[x - 2(k_{x,i} - 0.5)x_0\right]^2 + \left[y - 2(k_{y,i} - 0.5)y_0\right]^2}{2k_{\sigma,i}^2\sigma_0^2}\right\}. \end{aligned} \tag{7}$$

Consequently, the physical variables for ith injections, i.e, t_{wi}, V_i and (x_i, y_i), can be expressed explicitly as

$$t_{wi} = \frac{k_{\sigma,i}^2\sigma_0^2}{2D}, \tag{8a}$$

$$V_i = 2\pi\phi_0 k_{\phi,i}\sigma_0^2 k_{\sigma,i}^2, \tag{8b}$$

$$(x_i, y_i) = \left(2(k_{x,i} - 0.5)x_0, 2(k_{y,i} - 0.5)y_0\right). \tag{8c}$$

To optimize the treatment, a carefully selected set of criteria is employed. A crucial factor in this process is $CEM43$, which is used to assess the tumor ablation outcome. As mentioned in Section 2.3, cells are considered effectively destroyed when $CEM43$ exceeds 60 min. Additionally, a ceiling temperature of 46 °C is established to prevent the risk of irreversible denaturation of antigens and inflammatory

Table 1
Summary of the optimization parameters.

Variable	Independent parameter	Ratio	Reference	Relation
Volume fraction amplitude	ϕ_i	$k_{\phi,i}$	ϕ_0	$k_{\phi,i} = \phi_0/\phi$
Standard deviation	σ_i	$k_{\sigma,i}$	σ_0	$k_{\sigma,i} = \sigma_i/\sigma_0$
x coordinate	x_i	$k_{x,i}$	x_0	$k_{x,i} = x_i/2x_0 + 0.5$
y coordinate	y_i	$k_{y,i}$	y_0	$k_{y,i} = y_i/2y_0 + 0.5$
Centrosymmetric distance	d	k_d	d_0	$k_d = d/d_0$
Horizontal distance	d_h	k_{dh}	$1.25d_0$	$k_{dh} = d_h/(1.25d_0)$
Vertical distance	d_v	k_{dv}	$0.8d_0$	$k_{dv} = d_v/(0.8d_0)$
Inclined distance	d_β	$k_{d\beta}$	d_0	$k_{d\beta} = d_\beta/d_0$
Inclined angle	β	k_β	β_0	$k_\beta = \beta/\beta_0$
Treatment time		t_t		

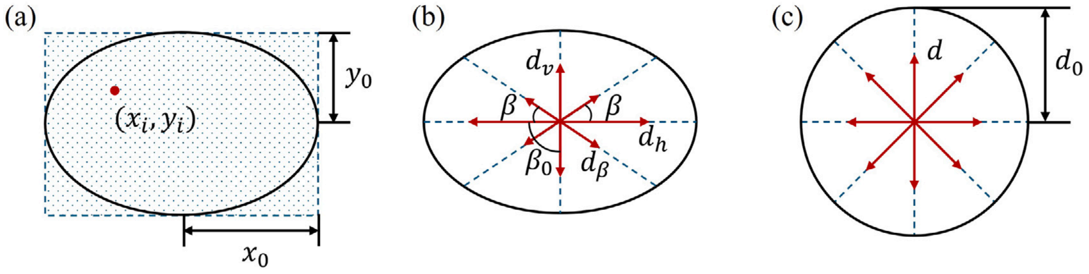

Fig. 2. Schematic of the parameter search in the optimization using (a) random search, (b) axisymmetric search, and (c) centrosymmetric search.

response [55–57]; meanwhile, the maximum temperature needs to approach 46 °C for efficient heating. Furthermore, the toxicity of MNPs should be taken into account. Minimizing the MNP dosage is essential to ensure safety and avoid side effects, such as deteriorating lung tissue and shortened lifespan, even though MNPs are generally of low toxicity [58,59]. Consequently, four requirements for evaluating the treatment efficacy of magnetic hyperthermia are summarized as

$$R_{CEM43} = \frac{S_{CEM43\ >\ 60\ \min in\ tumor}}{S_{tumor}}, \tag{9a}$$

$$R_{Tarea} = \min\left(\frac{S_{T<46^\circ\mathrm{C}\ in\ tumor}}{S_{tumor}}\right), \tag{9b}$$

$$R_{Tmax} = \exp\left(-\left|T_{max} - 46^\circ C\right|\right), \tag{9c}$$

$$R_{dose} = 1 - \sqrt[3]{\sum_{i=1}^{n} k_{\phi,i} k_{\sigma,i}^2}, \tag{9d}$$

where S denotes the area. R_{CEM43} records a ratio of the ablated region within the tumor, intuitively reflecting the treatment efficacy. R_{Tarea} represents the minimum ratio of the tumor area where the temperature remains below 46 °C throughout the entire treatment process. Overheating reduces this value. R_{Tmax} signifies the level of agreement between the maximum temperature T_{max}, both temporary and spatially, and the threshold temperature 46 °C. The collaboration of R_{Tarea} and R_{Tmax} is used to ensure that the maximum temperature during treatment approaches but remains below the inflammation threshold of 46 °C. R_{dose} evaluates the dosage requirement, as the total MNP volume is proportional to the accumulation of $k_{\phi,i}k_{\sigma,i}^2$. Ideally, the maximum value for each requirement variable is 1. The objective function J integrates the above considerations and is formulated as

$$J = \omega_1 R_{CEM43} + \omega_2 R_{Tarea} + \omega_3 R_{Tmax} + \omega_4 R_{dose}, \tag{10}$$

where $\omega_1 \sim \omega_4$ are weight coefficients, assigned values of 0.4, 0.3, 0.2, and 0.1 after conducting several trials, respectively, for emphasizing the efficacy and efficiency of the treatment. The objective function J roughly ranges in $[0, 1]$, with a higher value indicating better performance.

The PSO algorithm is applied to find the maximum value of the objective function J and to explore the optimal treatment strategy in this study. As a heuristic optimization algorithm, PSO is adept at handling large quantity variables without making assumptions [31,60,61]. Its effectiveness in optimizing magnetic hyperthermia treatment has been well-validated in our previous work [25].

Each scenario within the optimization process halts either when the ablation extends to healthy tissue or when the maximum treatment time is reached, which results in an optimal treatment time $t_{opt,t}$. Simultaneously, the optimization yields a set of optimal ratios, including k_ϕ, k_σ, and $(k_{x,i}, k_{y,i})$, for the initial MNP distribution. Based on these results, the optimal waiting time $t_{opt,wi}$, the optimal volume of MNPs $V_{opt,i}$, and the optimal injection sites $(x_{opt,i}, y_{opt,i})$ can be calculated by Eq. (8). Specifically, for symmetric MNP injections, the optimization outcomes provide the optimal distance, as $d_{opt,i} = k_{d,i}d_{0i}$. Subsequently, along the respective directions, the injection locations can be easily determined.

3. Results and discussions

In this work, the configuration asymmetry serves as the primary source of variation for investigating the optimal efficacy of magnetic hyperthermia, represented by the diversity of tumor models and the presence of blood vessels. The waiting time before AMF application is restricted to 20 min, and the maximum treatment duration is set as 120 min. To balance optimization convergence and computational time consumption, 30 particles and 100 generations in PSO are used for each optimization search.

3.1. Far from blood vessel

When the tumor is located far from the blood vessel, the effects induced by the blood flow can be neglected. Without this influence, the configuration is symmetrical but has divergent geometric variations. As described in Section 2.4, the injections are centrosymmetrically positioned around the tumor center in the circular tumors, with the identical initial MNP distribution and distance to the tumor center. In the elliptical tumor cases, the injections are axisymmetrically distributed along the major axis, minor axis, and inclined direction, with only the distance varying based on these three directions while

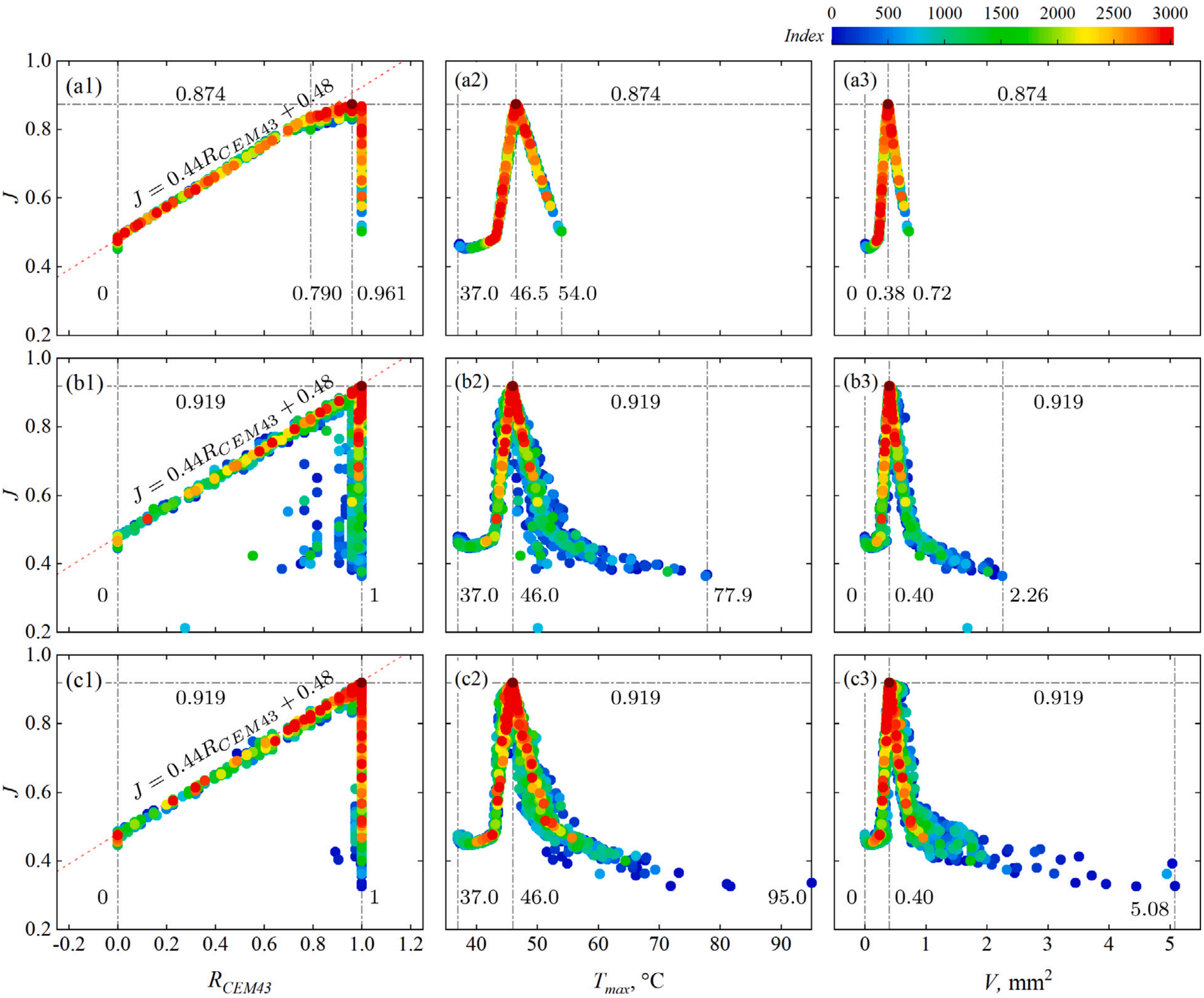

Fig. 3. Optimization trajectory of the circular tumor model, including the tumor ablation ratio R_{CEM43}, the appeared maximum temperature T_{max}, and the required volume of MNP V, in the scenarios of (a1)~(a3) one-site injection, (b1)~(b3) four-site injection, and (c1)~(c3) eight-site injection, respectively. The dark red point indicates the optimal choice.

maintaining the identical initial MNP distribution for each injection. Detailed discussions of the circular and elliptical tumor models are presented in Section 3.1.1 and Section 3.1.2, respectively.

3.1.1. Circular tumor

For the circular tumor, the optimization process is governed by four independent parameters: the treatment time (t_t) and three variables for initial MNP distribution (k_ϕ, k_σ, and k_d). The subscript "i" is omitted because the settings are identical for each injection. The corresponding reference parameters of the ratios are as follows: $\phi_0 = 0.05$, which ensures the applicability of the model for nanofluids [47] by preventing the MNP concentration from reaching excessively high levels; $\sigma_0 = 1.55$ mm, which is determined based on a 20 min waiting time limitation by solving Eq. (3); $d_0 = 5$ mm, which is used to define the injection area within the tumor. The optimization search considers scenarios involving one-site, four-site, and eight-site injections. The centrosymmetry requires $k_d = 0$ for the one-site injection.

Fig. 3 illustrates the optimization trajectory during the PSO search process for scenarios with various injection numbers, where J versus the physical variables (the tumor ablation ratio R_{CEM43}, the appeared maximum temperature T_{max}, and the required volume V of MNP) are presented. Since the PSO search iterates over 100 generations with 30 particles in each iteration, there are a total of 3030 possible choices for the entire optimization process, including an additional 30 particles for the initial choices. These particles are distinguished by color according to their respective generations. Each search begins with randomly generated independent ratios, i.e., k_ϕ, k_σ, and $(k_{x,i}, k_{y,i})$, which results in the roughly scattered across the entire potential range of the objective function J, represented by the dark blue points. As the generation increases, J approaches the optimal result.

In the case where no MNP is injected ($V = 0$ mm^2), the maximum temperature T_{max} should still remain 37 °C, which definitely leads to no ablation ($R_{CEM43} = 0$) in the tumor region. This observation holds true across all searches with various injection numbers and is illustrated in Fig. 3. On the contrary, an excess of MNPs easily ablates all the tumor tissue ($R_{CEM43} = 1$), but results in overheating ($T_{max} > 46$ °C). As the number of injections increases, the achieved MNP dose becomes larger, and the observed maximum temperature rises, especially during the initial search stage.

As shown in Figs. 3(a1), (b1), and (c1), an evident upward trend is observed for the objective function J versus the tumor ablation ratio R_{CEM43}. Surprisingly, all three relationships conform to the linear relationship $J = 0.44R_{CEM43} + 0.48$. Specifically, J approaches approximately 0.48 as R_{CEM43} approaches 0, with the corresponding T_{max} falling within the range of [42.3, 43.3] °C according to the raw data, and $R_{Tarea} = 1$ across all the options for each injection number, indicating no occurrence of overheating. The slope of 0.44 is greater than the weighting factor of 0.4 for R_{CEM43}, which unveils

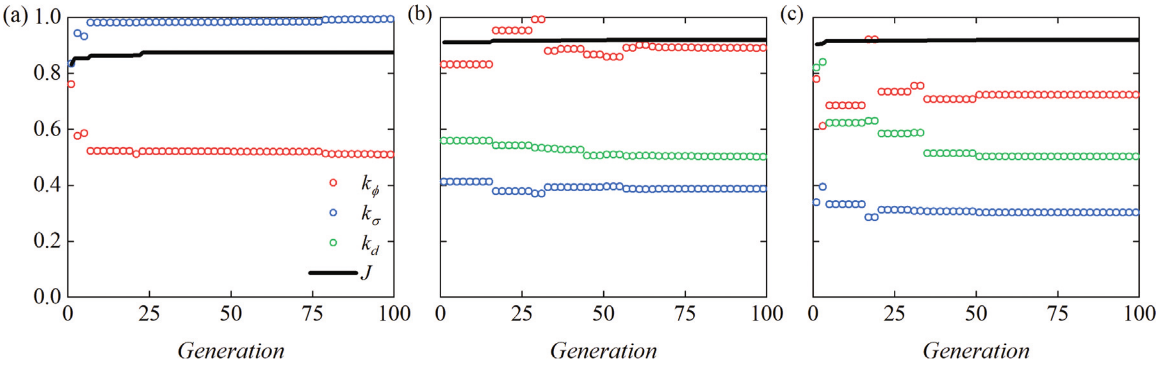

Fig. 4. Evolution of optimal parameter ratios and the corresponding objective function J on the circular tumor model, in the scenarios of (a) one-site injection, (b) four-site injection, and (c) eight-site injection.

Table 2
Optimization results of the objective function J and the corresponding requirements for the scenarios with one-site, four-site, and eight-site injections in the circular tumor model.

Injection strategy	R_{CEM43}	R_{Tarea}	R_{Tmax}	R_{dose}	J
One-site	0.961	0.931	0.950	0.204	0.874
Four-site	1.000	1.000	1.000	0.189	0.919
Eight-site	1.000	1.000	1.000	0.191	0.919

an additional increment of 0.04 in the slope generated by a positive correlation among ablation, temperature, and MNP dosage. Typically, a larger ablation area is associated with higher temperature, which requires more heat generated by the MNPs. However, the reduced slope for single-site injections after R_{CEM43} = 79.0% renders it less effective compared to the other two optimal outcomes. The peak value of the objective function J is attained at $R_{CEM43} = 1$ as expected, except in the case of the single-site injection, where R_{CEM43} = 96.1%. In contrast, for T_{max} (see Figs. 3(a2), (b2), and (c2)) and V (see Figs. 3(a3), (b3), and (c3)), the objective function increases to its peak from both sides. As revealed, the optimal T_{max} is 46.0 °C for both the four-site and eight-site injections, which is superior to the 46.5 °C observed for the single-site injection. Meanwhile, the optimal V values are 0.38 mm^2, 0.40 mm^2, and 0.40 mm^2 for the three approaches, respectively. Consequently, these results lead to a higher score in the objective function J (0.919) for both four-site and eight-site injections compared to the single-site injection (0.874).

Fig. 4 illustrates the PSO convergence process for single-site, four-site, and eight-site injections. It is evident that in all three scenarios, the objective function J nearly converges after 50 generations, with only minor adjustments in the parameters, indicating the rapid convergence of the current optimization setup for the circular tumor model. The convergence values of the objective function for the four-site and eight-site injection strategies reach the same levels, significantly outperforming that of the single-site injection strategy, which is consistent with the discussion in Fig. 3. The ratio k_ϕ depicted in Fig. 4 decreases as the injection number rises from four to eight, but the lowest value is observed in the scenario of a single-site injection, likely to mitigate the risk of overheating at the tumor center [25].

To further compare optimal outcomes across the three treatment strategies, Table 2 tabulates the optimal values for the four requirements and the objective function. The data clearly demonstrate the shortcomings of the one-site treatment strategy regarding overheating and tumor ablation issues, despite its slightly lower MNP dosage. $R_{T_{max}}$ = 0.950 and $R_{T_{area}}$ = 0.931 for the one-site strategy may account for its specificity. According to the formulations in Eq. (9), this combination reveals a deviation of the maximum temperature T_{max} from 46 °C, with overheating occurring in 6.9% of the tumor area, which is further confirmed by T_{max} = 46.5 °C observed in the one-site injection scenario (see Fig. 3(b2)). Additionally, R_{CEM43} = 0.961 indicates that 3.9% of the tumor tissue cannot be destroyed, even with the optimal one-site injection strategy. In contrast, the four-site and eight-site strategies successfully eliminate the entire tumor with optimal temperature evolution and the appropriate dose of MNP, making them both the preferred choices. The optimal treatment strategy for a single-site injection represents a compromise between overheating and complete ablation, resulting in a low k_ϕ due to this balance, as illustrated in Fig. 4. As the number of injections increases, the ratio k_σ decreases, indicating a reduction in the waiting time before AMF application. The value of k_d remains constant across both the four- and eight-site treatment strategies.

Consequently, the optimal treatment strategies for the four-site and eight-site injections are presented in Fig. 5. Note that, with the identical MNP volumes V_{opt}, the same treatment time $t_{opt,t}$ enables both strategies to achieve perfect treatment efficacy, despite a shorter waiting time $t_{opt,w}$ for the eight-site strategy.

3.1.2. *Elliptical tumor*

Given the axisymmetric configuration of the elliptical tumor model, the parameters for distance are assigned along the major axis (d_h), minor axis (d_v), and inclined direction (d_β). Consequently, the strategy optimization is governed by the treatment time t_t and six ratios: k_ϕ, k_σ, k_{dh}, k_{dv}, $k_{d\beta}$, and k_β, where the additional ratio $k_\beta = \beta/\beta_0$ is used for the inclined angle search. The reference values for ϕ_0 and σ_0 are consistent with those in the circular tumor model (see Section 3.1.1), while the reference distances are adjusted to $d_{h0} = 1.25d_0$, $d_{v0} = 0.8d_0$, and $d_{\beta 0} = d_0$, alongside $\beta_0 = 90°$. The search for one-, two-, four-, and eight-site injections is conducted, with arrangements for the ratios of distance gradually incorporating k_{dh}, k_{dv}, and $k_{d\beta}$ as the number of injection sites increases from two to eight.

Fig. 6 presents the optimization trajectories of the eight-site injections in the elliptical tumor models. Compared to the eight-site injections in the circular tumor model (see Figs. 3(c1)∼(c3)), the trajectories in both scenarios follow a similar search path and exhibit comparable trends. One major difference is that the increased search freedom, resulting from the separation of distance groups along different directions, allows for more possibilities (see Figs. 3(c1) and 6(a)). The maximum temperature T_{max} (77.9 °C, see Fig. 6(b)) and the maximum MNP dose V (5.7 mm^2, see Fig. 6(c)) observed in the elliptical tumor model during the optimization process also highlight the differences. Meanwhile, more points representing the lower objective function values are observed during the early search stage, but this does not impede the discovery of the optimal solution due to the strong search capability of PSO. This search also achieves perfect treatment efficacy (R_{CEM43}=1) and the ideal maximum temperature (T_{max} = 46.0 °C), along with a slightly increased demand for the MNP dose (V = 0.47 mm^2). The search trend in Fig. 6(a) continues to follow the fitting law observed in Fig. 3(c1), indicating that the optimization trend is applicable to different parameters and tumor shapes.

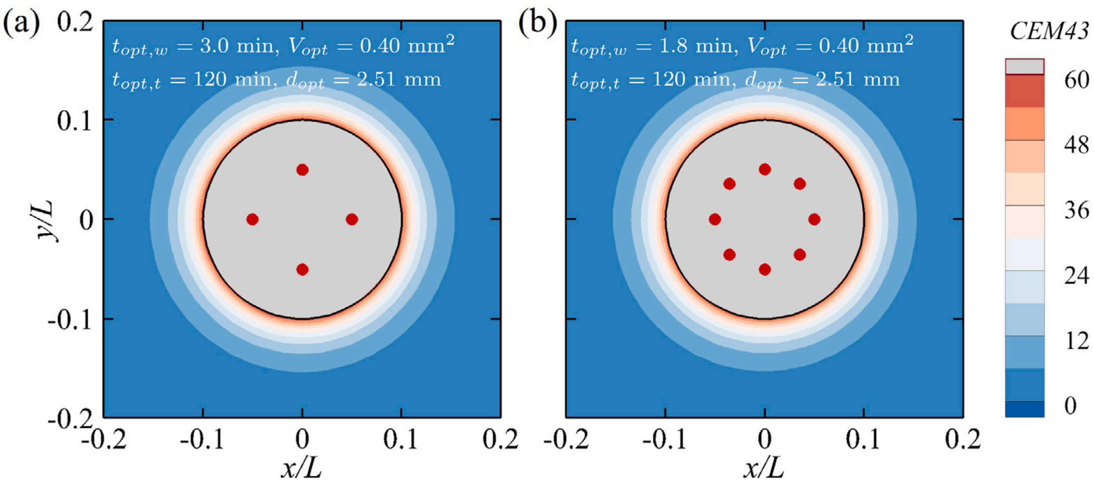

Fig. 5. Optimal treatment strategies for (a) four-site and (b) eight-site injections in the case of circular tumor models. The black solid line denotes the tumor boundary, while the gray region signifies the ablated area after the optimal treatment duration. The red points mark the locations of the injections.

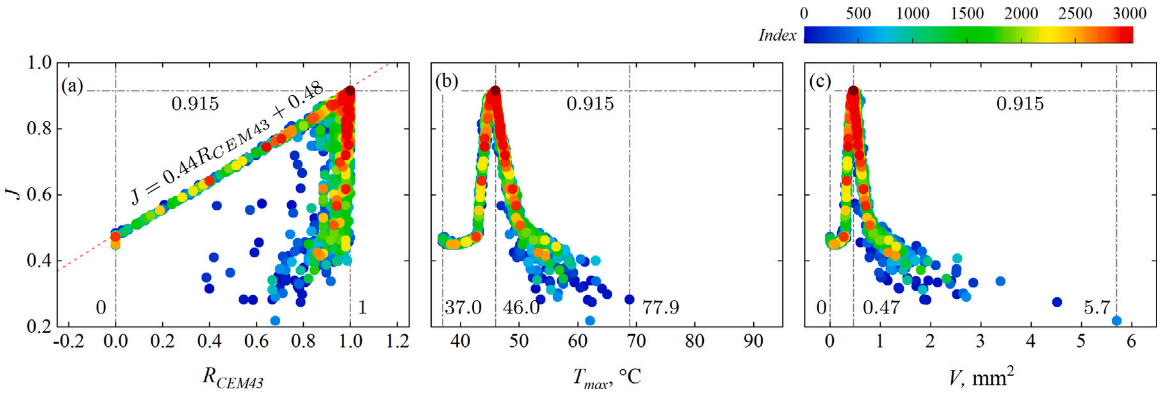

Fig. 6. Optimization trajectory during the PSO search process, including (a) the tumor ablation ratio R_{CEM43}, (b) the observed maximum temperature T_{max}, and (c) the required MNP volume V, in the scenarios of eight-site injection for elliptical tumor model. The dark red point indicates the optimal choice.

Table 3
Optimization results for the scenarios with the one-, two-, four- and eight-site injections in the elliptical tumor model.

Injection strategy	R_{CEM43}	R_{Tarea}	R_{Tmax}	R_{dose}	J
One-site	0.685	1.000	1.000	0.235	0.796
two-site	0.994	1.000	1.000	0.137	0.911
Four-site	0.949	1.000	1.000	0.158	0.895
Eight-site	1.000	1.000	1.000	0.147	0.915

The convergence processes of the PSO search for the elliptical tumor model with one-, two-, four-, and eight-site injections are shown in Fig. 7. Although the parameter ratios approach convergence slightly later compared to the circular tumor model, all the objective functions nearly converge before 70 generations across the four scenarios, which reflects the strong convergence performance of PSO. On the other hand, the delayed convergence of independent parameters emphasizes the multimodal nature of the problem, indicating that PSO is well-suited for addressing issues with marginal differences among local maxima. In these four scenarios, the eight-site injection converges to the highest value for the objective function J (0.915), followed sequentially by the two-site injection (0.911), four-site injection (0.895), and the one-site injection (0.796), as shown in Table 3. Indeed, all treatment strategies selected through optimization satisfactorily meet the temperature distribution requirements (R_{Tarea} and R_{Tmax}), while the primary variations arise in the ablation ratio R_{CEM43} and the MNP dose R_{dose}. The eight-site treatment strategy achieves the ideal ablation ratio (R_{CEM43} = 1), though it has a marginally inferior MNP dose. Surprisingly, the two-site strategy achieves up to 99.4% tumor ablation, only slightly inferior to the performance of the eight-site strategy. The four-site strategy demonstrates better performance in terms of MNP dose but leaves 5.1% of tumor cells surviving, while the one-site strategy can only ablate 68.5% of tumor cells. As a result, the eight-site strategy and the two-site strategy are considered more suitable for the treatment.

Hence, the two optimal treatment strategies using two-site and eight-site injections are presented in Fig. 8. For the eight-site treatment strategy, the optimal required MNP dose V_{opt} is 4.1% lower, while the waiting time before AMF application $t_{opt,w}$ and treatment duration $t_{opt,t}$ are 60.3% shorter and 14.8% longer, respectively, than the two-site strategy. Interestingly, all the injection sites are nearly aligned along the major axis. The horizontal and inclined sites are positioned close to the locations used in the two-site strategy, while the vertical sites almost reach the center of the tumor. Regarding tumor ablation, the small residual portions observed at the upper and lower tumor boundaries in the two-site strategy, which are absent in the eight-site strategy, indicate that the two vertical injections enhance the efficacy of the eight-site strategy in addressing the inadequate ablation associated with the two-site treatment.

Although the tumor area is identical for the two models, the optimal treatment strategies differ considerably. The eight-site treatment strategy serves as an illustrative example. The optimal MNP dose for the elliptical tumor model exceeds that of the circular tumor model by 17.5%. Meanwhile, the optimal injection sites for the circular tumor are arranged in a circle as predetermined (see Fig. 5) and undergo a

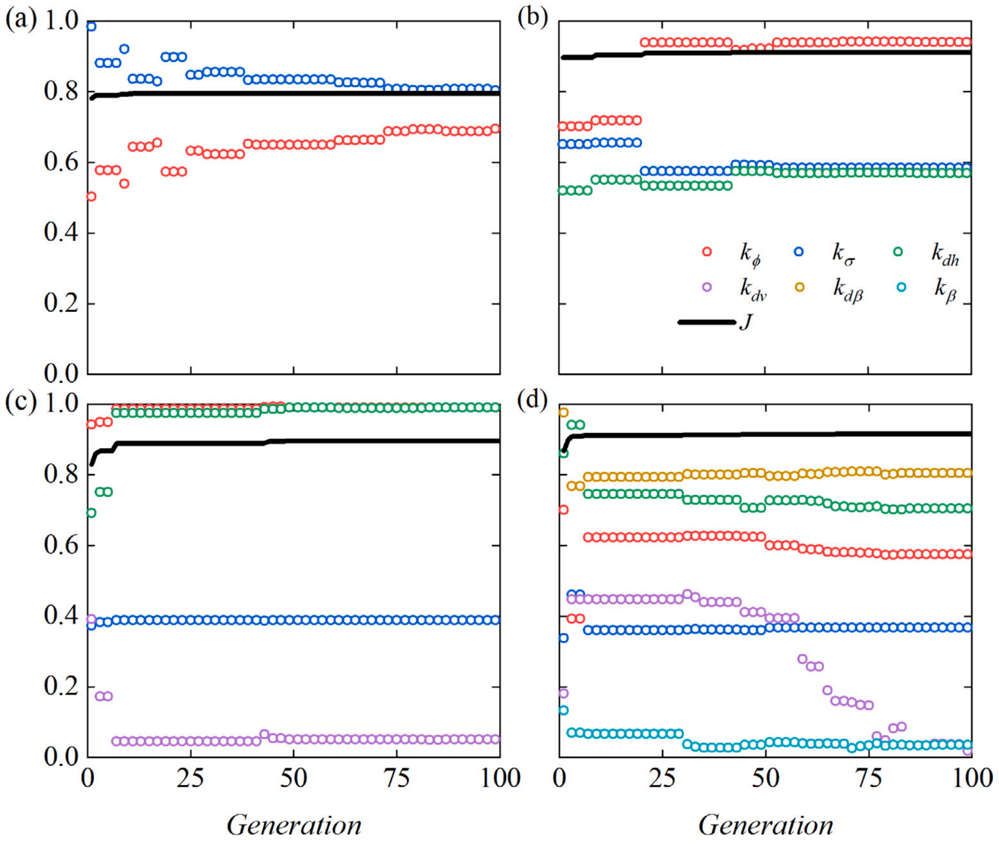

Fig. 7. Evolution of optimal parameter ratios and corresponding objective function J on the elliptical tumor model, in the scenarios of (a) one-site injection, (b) two-site injection, (c) four-site injection, and (d) eight-site injection.

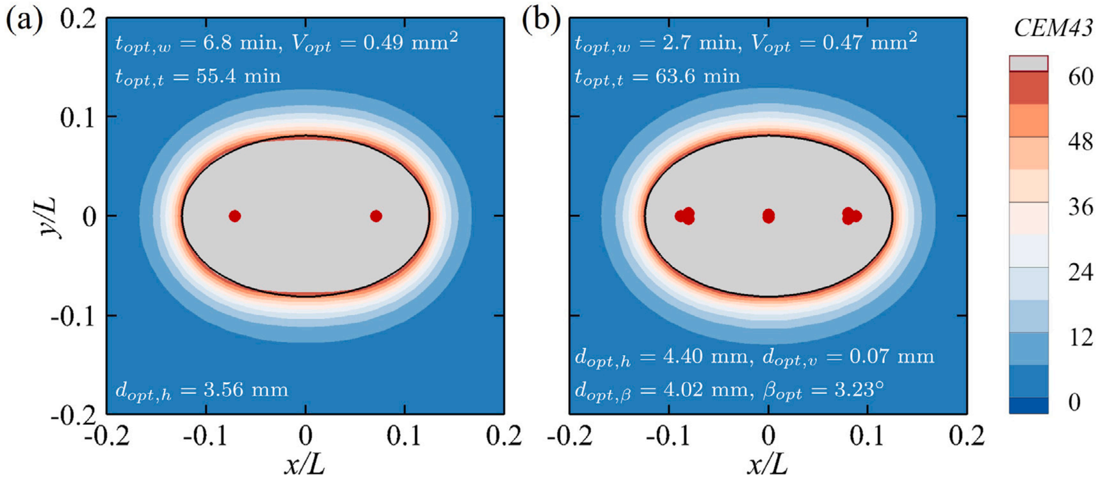

Fig. 8. Optimal treatment strategies for (a) two-site and (b) eight-site injections in elliptical tumor models. The black solid line denotes the tumor boundary, while the gray region signifies the ablated area after the optimal treatment duration. The red points indicate the locations of the injections.

120 min treatment, which meets the time limitation; conversely, the separated groups of injection sites for the elliptical tumor form an extremely elongated ellipse, resembling a line along the major axis (see Fig. 8), where the treatment time is approximately halved compared to the circular tumor model. These divergences can be attributed to MNP diffusion. In the circular tumor model, MNPs diffused from the centrosymmetric injection sites maintain centrosymmetry throughout the treatment. A longer treatment time ensures adequate MNP diffusion and more uniform MNP heating, resulting in a smoother ablation boundary. However, in the elliptical tumor model, MNP diffusion causes the ablation area to transition from a thinner to a thicker pattern [25]. Therefore, the line-like distribution of injections in the elliptical tumor model facilitates complete ablation.

The effectiveness of the present optimization study in the magnetic hyperthermia treatment is evident when compared with our previous work [25], in which treatment efficacy was evaluated based on temperature, and the MNP distribution is treated as static during the optimization process. Fortunately, the optimal choices for the circular tumor model (the four- and eight-site injection strategies) and the elliptical tumor model (the two- and eight-site injection strategies) are consistent with previous work [25]. However, the difference emerges in the optimal treatment efficacy, which is slight in the circular tumor

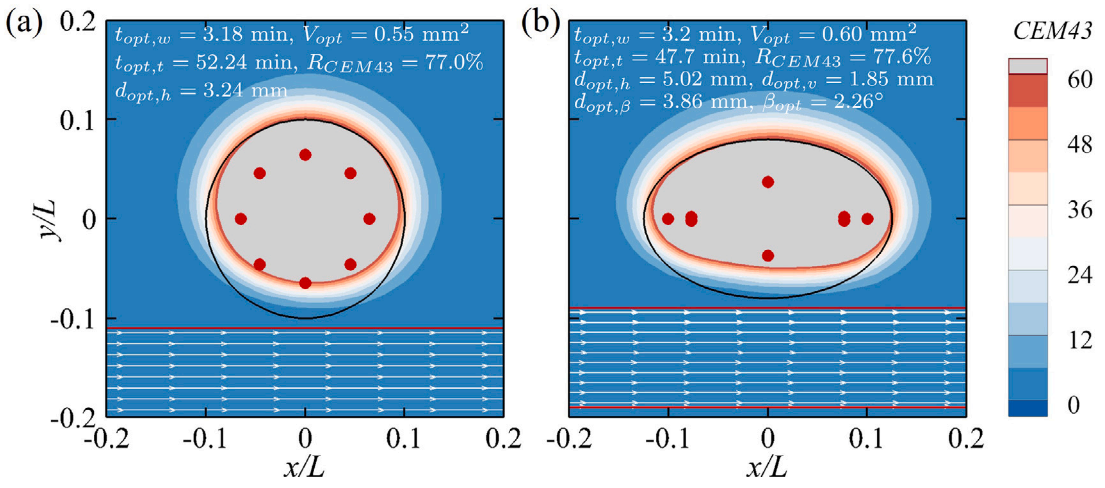

Fig. 9. Optimal treatment strategies for eight-site injections with vessel flow at $\delta = 1$ mm in (a) the circular tumor model and (b) the elliptical tumor model. The black solid line denotes the tumor boundary, while the gray region signifies the ablated area after the optimal treatment duration. The red points indicate the locations of the injections.

model but becomes more considerable in the elliptical tumor model. By incorporating the impact of treatment duration on MNP mass transfer and thermal dose, the treatment efficacy of the two- and eight-site strategies for the elliptical tumor model is enhanced by 4.2% and 11.4%, respectively. This indicates the suitability of the present arrangement for optimization and provides a more direct and precise approach to identifying optimal tumor ablation efficacy.

3.2. *Near blood vessel*

In practice, the effectiveness of magnetic hyperthermia treatment is notably affected by the cooling effect of the nearby blood vessel [52,62–65]. Therefore, this section incorporates a fully developed superficial venous flow characterized by a parabolic velocity profile and a constant central velocity of 1.0 mm/s [66,67], to evaluate its effects on optimal results and enhance treatment efficacy. Firstly, a comparison of the scenarios with and without the impact of the nearby blood vessel is presented in Section 3.2.1. Subsequently, a complete random search is employed to improve treatment efficacy and explore the impact of varying tumor–vessel distances in Section 3.2.2.

3.2.1. *Effect of vessel presence*

Firstly, we continue to adopt the symmetric injection distribution to assess the practical impact of an extremely nearby vessel with a tumor–vessel distance of $\delta = 1$ mm. The optimal eight-site treatment strategies for both circular and elliptical tumors are presented in Fig. 9. Compared with the scenarios without the blood vessel, the treatment efficacy deteriorates by 23.0% and 22.4% for the two tumor models, respectively, and the required MNP dose increases by 37.5% and 27.7%. The optimal treatment times $t_{opt,t}$ are both reduced, while concurrently, the injection sites move towards the tumor boundary.

It is evident from Fig. 9 that the vessel flow has a significantly asymmetric influence on tumor ablation. At their respective optimal treatment times $t_{opt,t}$ for the two models (52.2 min and 47.7 min), only 77.0% and 77.6% of the tumor tissues are destroyed. In the circular tumor model, the upper half ($y/L > 0$) contributes 62.3% of the total ablation area, while the lower half ($y/L < 0$) accounts for only 37.7%. Meanwhile, 52.3% of the ablation area comes from the right side ($x/L > 0$) and 47.4% from the left side ($x/L < 0$). Similar phenomena are also observed in the elliptical tumor model, which confirms the substantial cooling effect on the side of the vessel [38] and highlights the observable impact in the direction of the incoming flow. Consequently, the existence of the blood vessel and the blood flow form the asymmetric ablation shape. Hence, symmetric injections are no longer suitable for addressing this asymmetric issue, necessitating the implementation of the random search method for each injection.

Therefore, in the following optimization process, all parameters for each injection are independently adjusted. The determination of the ith injection relies on four ratios: $k_{\phi,i}$, $k_{\sigma,i}$, $(k_{x,i}, k_{y,i})$, so the n-site treatment strategy is governed by $4n$ ratios and a treatment time t_t. Based on the asymmetric configuration and preliminary investigations in the elliptical tumor model, the two-, four-, and eight-site injections are considered for discussion. The reference parameters ϕ_0 and σ_0 remain unchanged for ease of comparison, while the injection sites are directly determined by the locations (x, y), with the reference coordinate $(x_0, y_0) = (6.25, 4.0)$ mm. This ensures all injections are located within a rectangle tangential to the elliptical tumor boundary.

Fig. 10 illustrates the convergence process of the optimization, with all parameters freely adjustable during the search. The objective function converges within 80 generations across all three scenarios, while the individual parameter ratios continue to undergo slight adjustments. This further demonstrates the capability of PSO in effectively managing the substantial number of parameters in this multimodal problem.

Fig. 11 illustrates the optimization trajectories for the eight-site injections at $\delta = 1$ mm, including both symmetric and random searches. Intuitively, the vessel flow leads to incomplete ablation for all the options throughout the entire optimization process, with the observed maximum R_{CEM43} being only 0.946 and 0.939 for symmetric and random injections, respectively. Such findings align with Shih et al. [62], who noted inadequate heating in the tumor and excessive overheating in healthy tissue near the vessel flow. Fortunately, the transition from the symmetric search approach to the random search technique results in a substantial improvement in optimal thermal dose R_{CEM43} by 16.3% (see Fig. 11(a1) and (b1), where the optimal R_{CEM43} values are 77.6% and 93.9%, respectively), which significantly contributes to the increase in the objective function J (rising from 0.818 to 0.875). Nevertheless, the higher ablation ratio requires a larger MNP dose, which rises from 0.6 to 0.78 mm^2, as depicted in Fig. 11(a3) and (b3).

3.2.2. *Effect of tumor–vessel distance*

This section aims to provide improved treatment strategies for different tumor–vessel distances δ and examine the variation trends among these optimal outcomes. It is evident from Table 4 that the impact of vessel flow on treatment efficacy notably varies with the tumor–vessel distance δ, especially at short distances. At $\delta = 1$ mm, 10.5% of tumor cells remain unharmed by the optimal two-site treatment strategy. This percentage decreases as the number of injections increases. Specifically, 7.0% and 6.1% of areas in the tumor region

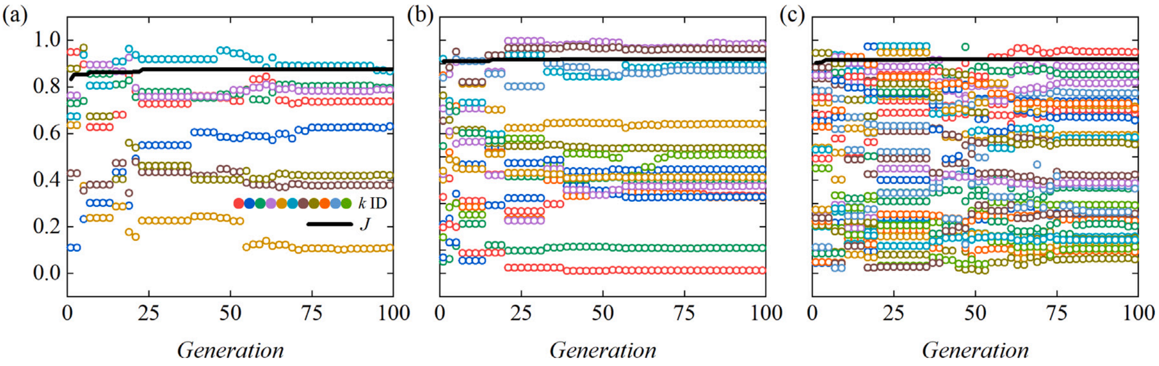

Fig. 10. Evolution of optimal parameter ratios and the corresponding objective function J at $\delta = 1$ mm in the elliptical tumor model, with (a) two-site injection, (b) four-site injection, and (c) eight-site injection.

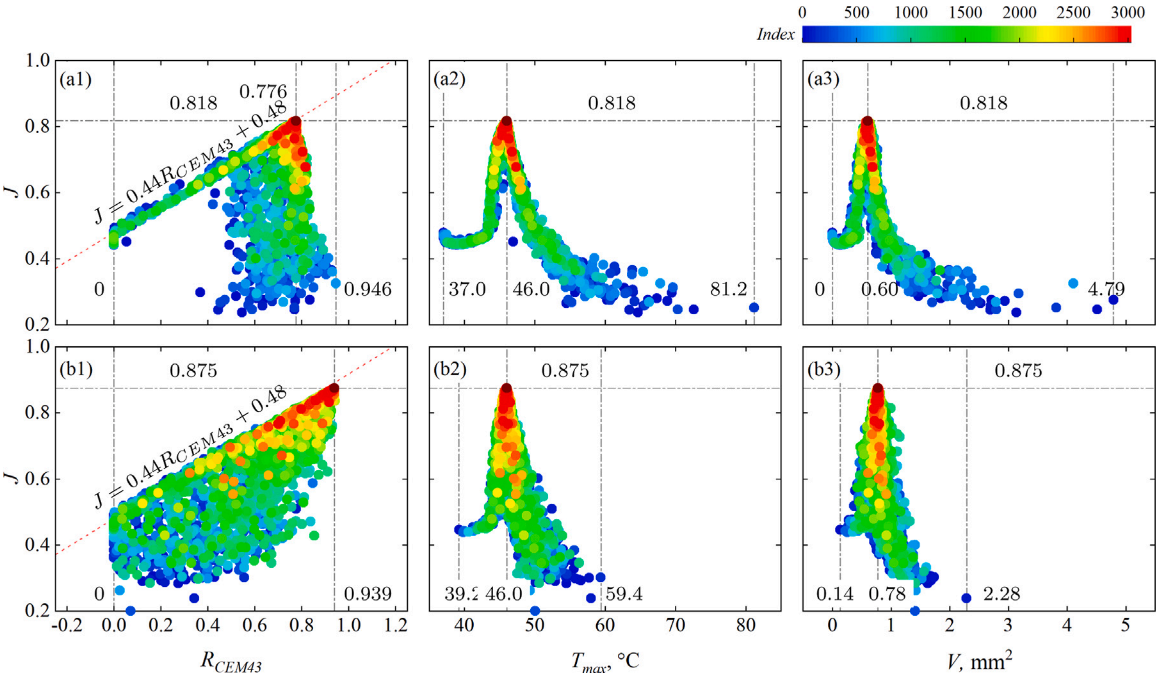

Fig. 11. Optimization trajectory at $\delta = 1$ mm in the elliptical tumor model, including the tumor ablation ratio R_{CEM43}, the observed maximum temperature T_{max}, and the required MNP volume V, in the scenarios of (a1)~(a3) symmetric eight-site injection, and (b1)~(b3) random eight-site injection, respectively. The dark red point indicates the optimal choice.

Table 4
Optimization results for the scenarios of two-, four-, and eight-site injections with the influence of vessel flow on the elliptical tumor model.

Injection strategy	δ, mm	J	R_{CEM43}	T_{max}, °C	$t_{opt,t}$, min	V_{opt}, mm^2
Two-site	1	0.862	0.895	46.0	120.0	0.64
	7	0.906	0.987	46.0	74.4	0.52
Four-site	1	0.876	0.930	46.0	110.4	0.66
	4	0.897	0.974	46.0	78.3	0.60
	7	0.900	0.974	46.0	65.9	0.54
	10	0.905	0.981	46.0	66.2	0.50
	13	0.908	0.987	46.0	65.2	0.49
Eight-site	1	0.874	0.939	46.0	85.8	0.78
	7	0.903	0.980	46.0	66.7	0.54

remain unaffected by the optimal four-site and eight-site treatment strategies, respectively. Given the considerable enhancement in the objective function when the number of injections increases from two-site to four-site, but with no further improvement at eight-site, the four-site injections receive greater emphasis for subsequent comparisons. In addition to the common distances of $\delta = 1$ mm and 7 mm for all the injections, distances of $\delta = 4$ mm, 10 mm, and 13 mm are specifically investigated in the four-site injection. For the four-site strategies, a noticeable enhancement in tumor ablation ratio R_{CEM43} occurs as δ extends to 4 mm, but only a slight increase is observed as δ further increases. Generally, the optimal required treatment duration $t_{opt,t}$ is notably longer at $\delta = 1$ mm compared with other distances and decreases with an increase in the injection number. A similar decreasing trend is observed in the optimal MNP dose V_{opt} with δ, while it shows an increasing trend with the injection number n.

Fig. 12 summarizes the optimal physical variables influenced by the injection number n and the tumor–vessel distance δ, including the optimal treatment duration $t_{opt,t}$, the optimal required MNP dose V_{opt}, and the optimal dose-weighted average injection sites ($(\bar{x}/L)_{opt}$, $(\bar{y}/L)_{opt}$). The optimal dose-weighted average injection sites for n-site injections are determined by: $\bar{x} = \sum_{i=1}^{n} x_i V_i / \sum_{i=1}^{n} V_i$ and $\bar{y} = \sum_{i=1}^{n} y_i V_i / \sum_{i=1}^{n} V_i$, revealing the centroid of the total MNP distribution. Evidently, $((\bar{x}/L)_{opt}, (\bar{y}/L)_{opt}) = (0, 0)$ for symmetrical injection. It can be seen that the average injection sites shift significantly downwards and slightly leftwards, following the position of the vessel and the direction of the incoming flow. The greatest deviation is detected at $\delta = 1$ mm

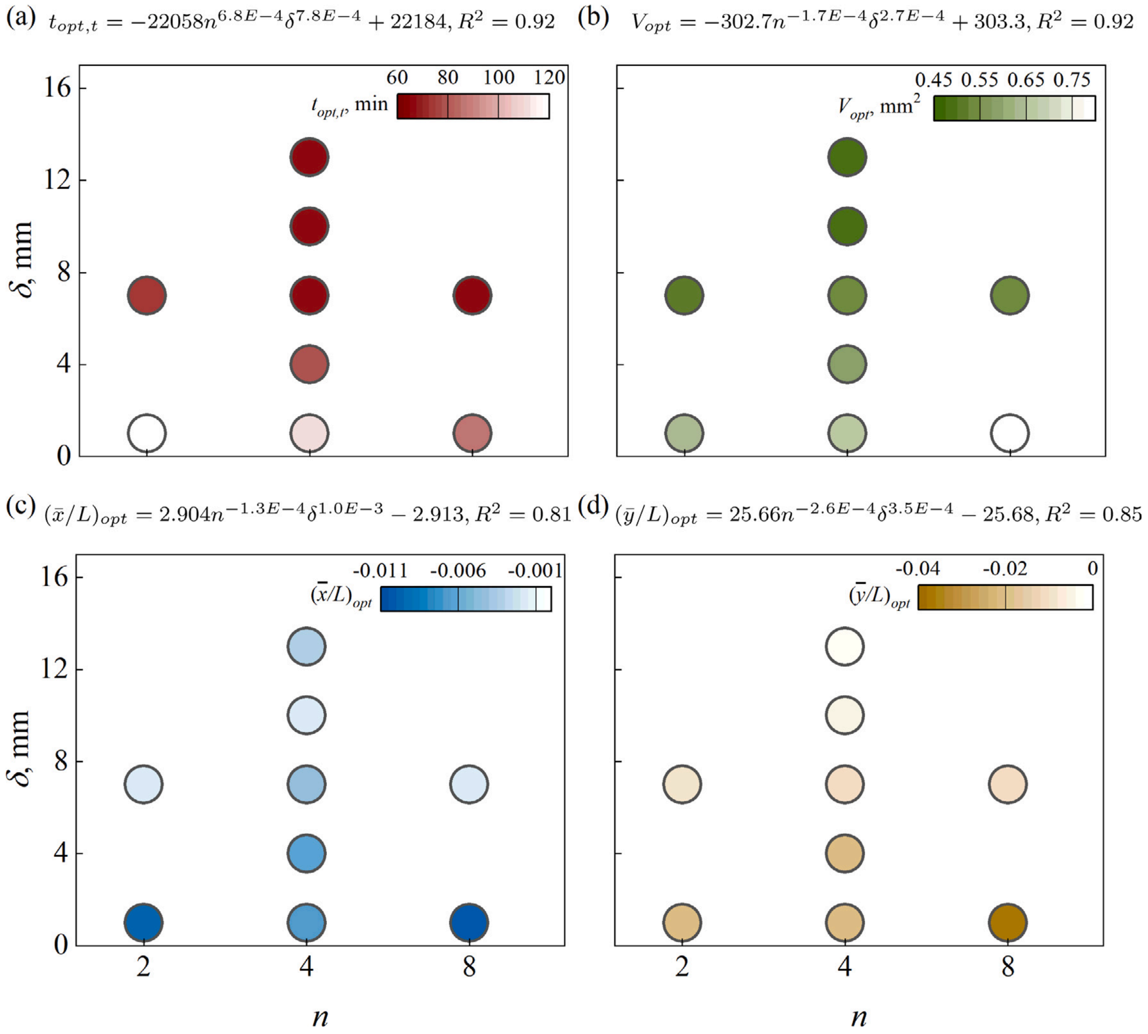

(a) $t_{opt,t} = -22058n^{6.8E-4}\delta^{7.8E-4} + 22184, R^2 = 0.92$

(b) $V_{opt} = -302.7n^{-1.7E-4}\delta^{2.7E-4} + 303.3, R^2 = 0.92$

(c) $(\bar{x}/L)_{opt} = 2.904n^{-1.3E-4}\delta^{1.0E-3} - 2.913, R^2 = 0.81$

(d) $(\bar{y}/L)_{opt} = 25.66n^{-2.6E-4}\delta^{3.5E-4} - 25.68, R^2 = 0.85$

Fig. 12. Variation of optimal physical variables with increasing injection number n and tumor–vessel distance δ for the elliptical tumor model, including the variables of (a) optimal treatment duration $t_{opt,t}$, (b) optimal MNP dose V_{opt}, (c) optimal average x-coordinate $(\bar{x}/L)_{opt}$, and (d) optimal average y-coordinate $(\bar{y}/L)_{opt}$.

by the eight-site strategy, with $((\bar{x}/L)_{opt}, (\bar{y}/L)_{opt}) = (-0.010, -0.038)$, representing 4.0% of the major axis and 23.8% of the minor axis, respectively. The fitting laws behind these variables are also provided as a valuable tool for predicting and evaluating treatment strategies.

For the optimal MNP dose, two injections significantly outweigh the others in each scenario, as illustrated in Fig. 13. In addition to the two major injections, there are two minor injections in the four-site strategy and four minor injections in the eight-site strategy. However, the cumulative dosage of the minor injections remains lower than that of each major injection. The major injections serve as the dominant heat source, while the minor injections compensate for the inadequate ablation, as presented in Fig. 14. Fig. 14 shows the optimal tumor ablation efficacy at $\delta = 1$ mm and 7 mm. The role of minor injections is noticeable at $\delta = 1$ mm, where a visible expansion of the ablation zone is observed, increasing from 89.5% for two-site injections to 93.0% for four-site injections, and finally to 93.9% for eight-site injections (see Figs. 14(a1)–(c1)). Comparatively, the four-site injection strategy is more suitable because the efficacy is significantly improved with the inclusion of two additional injections, though it is only marginally inferior to the eight-site strategy by 0.9% in tumor ablation area. Alternatively, if time and MNP toxicity permit, the eight-site strategy could be considered. However, such enhancement is less pronounced at $\delta = 7$ mm, where all cases achieve around 98.0% ablation in the tumor region (see Figs. 14(a2)–(c2)). Consequently, the two-site treatment

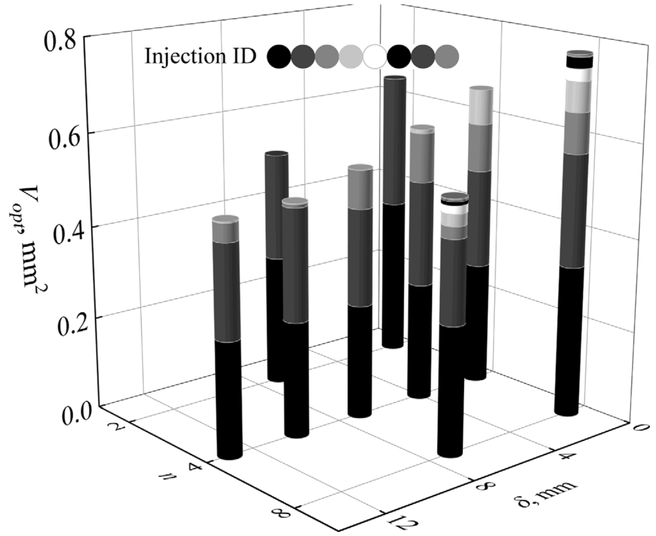

Fig. 13. Accumulation of optimal MNP dose for the elliptical tumor model.

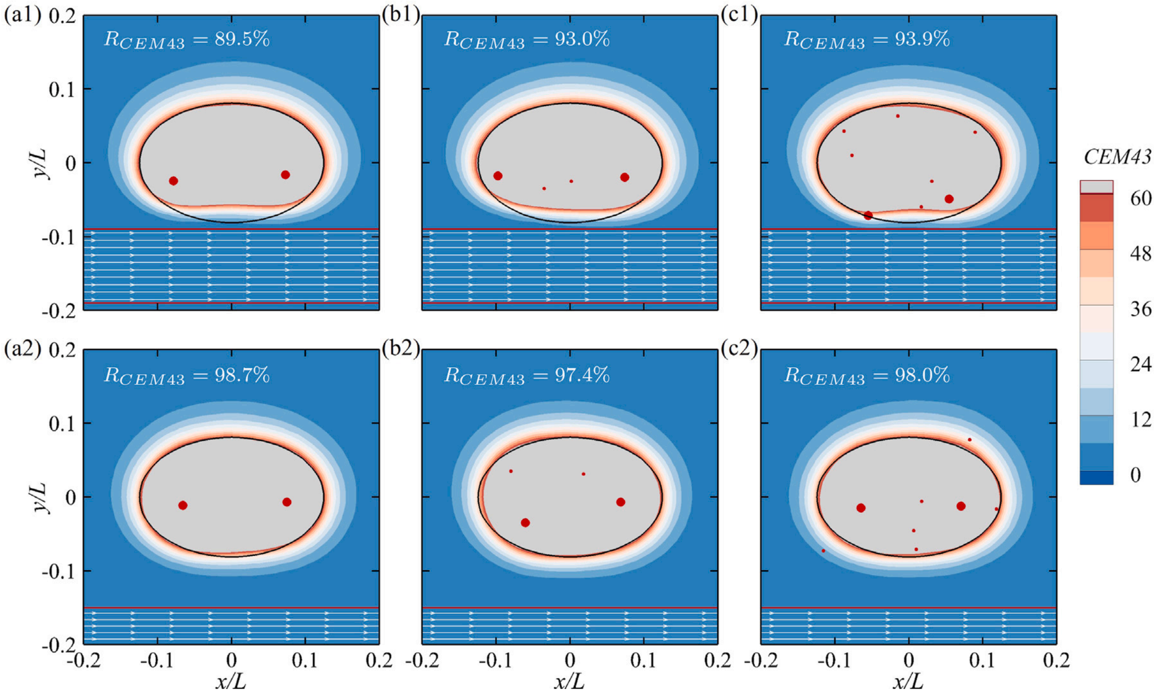

Fig. 14. The optimal treatment strategies for the elliptical tumor model with the cases of (a) two-site injection (b) four-site injection and (c) eight-site injection, at (a1)~(c1) $\delta = 1$ mm and (a2)~(c2) $\delta = 7$ mm. The black solid line denotes the tumor boundary. The red horizontal line denotes the upper vessel boundary, and the streamlines indicate the flow direction. The gray region means the ablated part, and the red point means the injection sites, with the large points for major injections and the small points for minor injections.

strategy is a suitable choice for both efficacy and convenience at $\delta = 7$ mm, which is consistent with the findings in the scenario when the tumor is distant from the vessel flow, as discussed in Section 3.1.2. Another concern arises regarding treatment efficacy when the tumor is close to the blood vessel, i.e., the cooling effect from the vessel flow creates a resistant area. In the case presented in Fig. 14(c1), despite the increased injection number and the use of asymmetric injections, the maximum temperature during treatment at the lower tumor boundary reaches only 41 °C, which is 1.8°C lower than at the upper boundary. However, although the cooling effects induced by the blood flow degrade the treatment efficacy of magnetic hyperthermia, it can still ablate 93.0% and 93.9% of tumor region with four- and eight-site injections, respectively, at $\delta = 1$ mm, which is significantly more effective than the surgical efficacy [68–70].

4. Conclusions

In this work, we investigate optimal tumor ablation outcomes in magnetic hyperthermia by incorporating the thermal exposure time, MNP dose, injection sites, and waiting time before AMF application into the optimization process, where we highlight the exposure time owing to its significance in MNP mass transfer and efficacy evaluation. Temperature and MNP volume fraction are assessed using the PBHTE and concentration equation, respectively, while optimal results are obtained through the PSO algorithm. Multi-site injections are employed in both circular and elliptical tumor configurations, and the notably asymmetric cooling effect induced by the nearby positioned blood flow is considered in this framework.

The rapid convergence across all scenarios indicates the suitability and effectiveness of the current optimization framework in identifying optimal treatment strategies for magnetic hyperthermia. Without the influence of blood flow, both the four-site and eight-site treatment strategies achieve the best performance in the circular tumor model, completely satisfying thermal dose and temperature requirements while using minimal MNP dose. In the elliptical tumor model, the eight-site treatment strategy outperforms the others, closely followed by the two-site strategy. The optimal eight-site injections exhibit a circular distribution as predetermined for the circular tumor model, while a linear distribution along the major axis, accompanied by approximately half the treatment duration for the elliptical tumor model. Notably, the incorporation of treatment duration in this study introduces significant refinements to the optimization strategy, markedly enhancing tumor ablation efficacy, particularly for the elliptical tumor model, resulting in complete satisfaction of the thermal dose for the eight-site strategy.

The presence of nearby blood flow introduces significant thermal asymmetry into the configuration, which adversely affects tumor ablation outcomes. In contrast, the random search technique for independent parameters demonstrates greater effectiveness in managing such asymmetric configurations compared to the symmetric search approach, resulting in a notable enhancement in optimal treatment efficacy. At tumor–vessel distance $\delta = 1$ mm, the optimal eight-site injection strategy demonstrates superior tumor ablation in the elliptical tumor model, achieving 93.9% tumor destruction. However, this strategy requires a larger MNP dose, which increases the risk of toxicity. In comparison, the optimal four-site treatment strategy effectively reduces biological toxicity, resulting in a value of the objective function that is nearly identical to that of the eight-site strategy, despite a slight degradation in tumor ablation. Therefore, the four-site injection strategy is more suitable and efficient. As δ increases to 4 mm, there is a visible improvement in tumor ablation with the four-site treatment strategy, achieving approximately 98% ablation in the tumor region, while the efficacy marginally improves with further increases in δ. During the enlargement of δ, the optimal treatment duration, required MNP dosage, and deviation of the average injection sites decrease. The numerical results also reveal two dominant MNP injections, which both exceed the cumulative dose of all minor injections. These two major injections serve as the primary heat sources during treatment, while the others compensate for insufficient ablation.

In conclusion, the present work provides effective approaches to achieve optimal ablation efficacy for tumors characterized by variations in configuration asymmetry. Despite the simplified two-dimensional

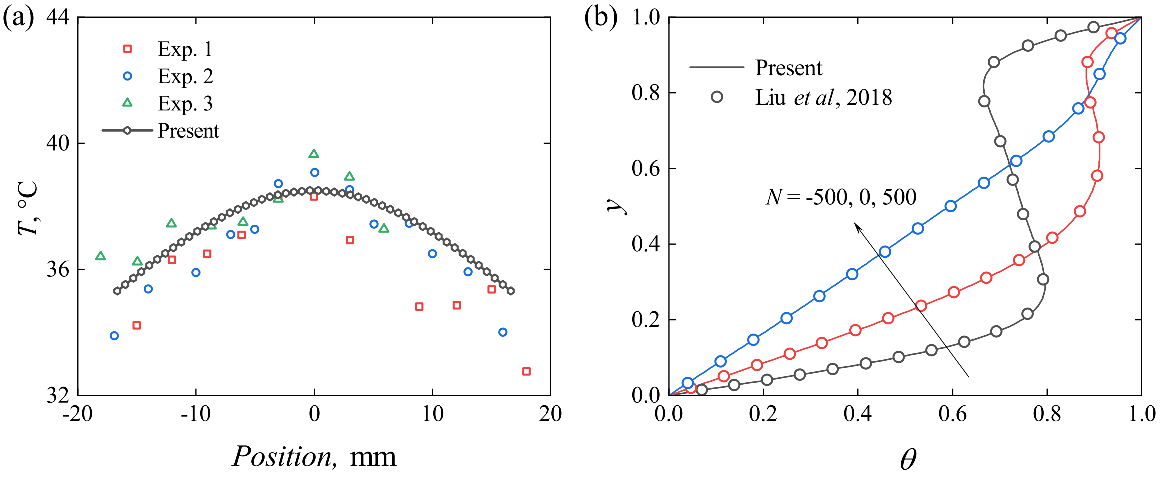

Fig. A.1. Validation of the present framework. Panel (a) compares the temperature profile obtained from our framework with the experimental results from rat studies on magnetic hyperthermia [71]. Panel (b) presents the dimensionless temperature profiles for the double-diffusive convection problem, validating the integration of the flow, temperature, and concentration fields, where θ denotes the dimensionless temperature [50].

setup, key factors are investigated through comprehensive numerical experiments, and the revealed mechanisms and relationships can provide optimal strategies for practical tumor ablation applications. However, due to length limitations, further discussion on more topics such as the effects of blood flow rate, flow pulsation, and real tumor shapes will be addressed in future work.

CRediT authorship contribution statement

Buchen Wu: Writing – review & editing, Writing – original draft, Visualization, Funding acquisition, Formal analysis. **Qian Jiang:** Writing – review & editing, Writing – original draft, Visualization, Validation, Software, Methodology, Investigation, Formal analysis. **Zhaokun Wang:** Writing – review & editing, Methodology. **Chenglei Wang:** Methodology. **Feng Ren:** Software. **Hui Tang:** Writing – review & editing, Funding acquisition, Conceptualization.

Declaration of competing interest

The authors declare that they have no known competing financial interests or personal relationships that could have appeared to influence the work reported in this paper.

Acknowledgments

This study was financially supported by the Research Grants Council of Hong Kong under General Research Fund (Project No. 15214418). Hui Tang would also like to acknowledge the support from Scientific Research Special Foundation of Jiangsu Province (No. BZ2024063). Buchen Wu acknowledges the fund from National Natural Science Foundation of China (No. 52478321).

Appendix. Validation of the framework

To ensure the reliability of the results presented in this work, this section demonstrates the validation of the numerical framework. As an extension of our previous study [25], which focused on optimizing the temperature distribution for magnetic hyperthermia by utilizing the “freezing time” during treatment, this work further develops the framework by incorporating additional modules for the MNP mass transfer and the impact of blood flow. The modules for temperature distribution governed by PBHTE and the optimization algorithm have already been well validated in our previous work [25]. Specifically, the validation of the temperature field is based on an in vivo experimental study by Salloum et al. [71], which investigates the temperature variation in the muscle tissue of a rat during magnetic hyperthermia. Fig. A.1(a) demonstrates that the simulated temperature falls almost entirely within the envelope defined by the three experimental data groups, indicating satisfactory agreement with the reference measurements, despite a minor deviation observed near the right boundary. The maximum error occurs at a position of 5.92 mm, where the temperature difference is 0.73 °C, corresponding to a 1.96% relative error with respect to the experimental envelope. In fact, the present LBM framework for the temperature field can solve Eq. (1c) with second-order accuracy [50], and the mesh resolution is sufficient for addressing the magnetic hyperthermia problem [25]. Consequently, the discrepancy with the experiment is primarily attributable to measurement uncertainty and model simplifications. On one hand, individual differences among the experiments, such as thermal properties, dynamic properties, and operational conditions, may introduce substantial uncertainty. On the other hand, treating the computational domain as homogeneous tissue represents another source of error; despite the minor variation in thermal properties across the real tissue block, these heterogeneities may influence the outcomes. Regarding the evolution of injected MNP, governed by Eq. (1), it follows a similar diffusion–convection equation as that for the temperature field. Both fields are solved using the D2Q5; thus, the validation of the temperature field also supports the validity of the MNP concentration field. Additionally, the integration of both temperature and concentration fields with the flow field, governed by the equations presented in Eq. (1), results in a typical double-diffusive convection problem. Consequently, a comparison with the numerical results for double-diffusive convection by Liu and He [72] is illustrated in Fig. A.1(b). In this scenario, the flow is driven by a moving lid and the buoyancy forces arising from both temperature and concentration gradients. The strong alignment with the reference results indicates the reliability and effectiveness of the numerical framework employed in this study.

Data availability

Data will be made available on request.

References

[1] R. Gilchrist, R. Medal, W.D. Shorey, R.C. Hanselman, J.C. Parrott, C.B. Taylor, Selective inductive heating of lymph nodes, Ann. Surg. 146 (4) (1957) 596.

[2] C.-T. Lin, K.-C. Liu, Estimation for the heating effect of magnetic nanoparticles in perfused tissues, Int. Commun. Heat Mass Transfer 36 (3) (2009) 241–244.

[3] M.A. Giordano, G. Gutierrez, C. Rinaldi, Fundamental solutions to the bioheat equation and their application to magnetic fluid hyperthermia, Int. J. Hyperth. 26 (5) (2010) 475–484.

[4] M. Szwed, A. Marczak, Application of nanoparticles for magnetic hyperthermia for cancer treatment—the current state of knowledge, Cancers 16 (6) (2024) 1156.

[5] L. Zhang, Q. Li, J. Liu, Z. Deng, X. Zhang, N. Alifu, X. Zhang, Z. Yu, Y. Liu, Z. Lan, et al., Recent advances in functionalized ferrite nanoparticles: from fundamentals to magnetic hyperthermia cancer therapy, Colloids Surf. B (2024) 113754.

[6] J. Ma, X. Yang, Y. Sun, J. Yang, Theoretical investigation on the thermo-mechanical responses of the human skin during thermal therapy, Int. J. Mech. Sci. 161 (2019) 105041.

[7] B. Rodriguez, D. Rivera, J.Y. Zhang, C. Brown, T. Young, T. Williams, S. Huq, M. Mattioli, A. Bouras, C.G. Hadjpanayis, Magnetic hyperthermia therapy for high-grade glioma: a state-of-the-art review, Pharmaceuticals 17 (3) (2024) 300.

[8] P. Das, M. Colombo, D. Prosperi, Recent advances in magnetic fluid hyperthermia for cancer therapy, Colloids Surf. B 174 (2019) 42–55.

[9] C.S. Kumar, F. Mohammad, Magnetic nanomaterials for hyperthermia-based therapy and controlled drug delivery, Adv. Drug Deliv. Rev. 63 (9) (2011) 789–808.

[10] S. Laurent, S. Dutz, U.O. Häfeli, M. Mahmoudi, Magnetic fluid hyperthermia: focus on superparamagnetic iron oxide nanoparticles, Adv. Colloid Interface Sci. 166 (1–2) (2011) 8–23.

[11] M. Liangruksa, R. Ganguly, I.K. Puri, Parametric investigation of heating due to magnetic fluid hyperthermia in a tumor with blood perfusion, J. Magn. Magn. Mater. 323 (6) (2011) 708–716.

[12] D. Chang, M. Lim, J.A. Goos, R. Qiao, Y.Y. Ng, F.M. Mansfeld, M. Jackson, T.P. Davis, M. Kavallaris, Biologically targeted magnetic hyperthermia: potential and limitations, Front. Pharmacol. 9 (2018) 831.

[13] M. Suto, Y. Hirota, H. Mamiya, A. Fujita, R. Kasuya, K. Tohji, B. Jeyadevan, Heat dissipation mechanism of magnetite nanoparticles in magnetic fluid hyperthermia, J. Magn. Magn. Mater. 321 (10) (2009) 1493–1496.

[14] A.-H. Lu, E.e. Salabas, F. Schüth, Magnetic nanoparticles: synthesis, protection, functionalization, and application, Angew. Chem. Int. Ed. 46 (8) (2007) 1222–1244.

[15] M. Peiravi, H. Eslami, M. Ansari, H. Zare-Zardini, Magnetic hyperthermia: Potentials and limitations, J. Indian Chem. Soc. 99 (1) (2022) 100269.

[16] R.E. Rosensweig, Heating magnetic fluid with alternating magnetic field, J. Magn. Magn. Mater. 252 (2002) 370–374.

[17] J. Dieckhoff, D. Eberbeck, M. Schilling, F. Ludwig, Magnetic-field dependence of Brownian and Néel relaxation times, J. Appl. Phys. 119 (4) (2016) 043903.

[18] A.E. Deatsch, B.A. Evans, Heating efficiency in magnetic nanoparticle hyperthermia, J. Magn. Magn. Mater. 354 (2014) 163–172.

[19] Y.-D. Tang, J. Zou, R.C. Flesch, T. Jin, Effect of injection strategy for nanofluid transport on thermal damage behavior inside biological tissue during magnetic hyperthermia, Int. Commun. Heat Mass Transfer 133 (2022) 105979.

[20] Q. Jiang, F. Ren, C. Wang, Z. Wang, G. Kefayati, S. Kenjeres, K. Vafai, X. Cui, Y. Liu, H. Tang, Multiphysics simulation of tumor ablation in magnetic hyperthermia treatment, Int. J. Heat Mass Transfer 245 (2025) 126982.

[21] Y. Tang, T. Jin, R.C. Flesch, Y. Gao, M. He, Effect of nanofluid distribution on therapeutic effect considering transient bio-tissue temperature during magnetic hyperthermia, J. Magn. Magn. Mater. 517 (2021) 167391.

[22] J. Crank, The Mathematics of Diffusion, Oxford University Press, 1979.

[23] A.A. Golneshan, M. Lahonian, Diffusion of magnetic nanoparticles in a multi-site injection process within a biological tissue during magnetic fluid hyperthermia using lattice Boltzmann method, Mech. Res. Commun. 38 (6) (2011) 425–430.

[24] G. Singh, N. Kumar, P.K. Avti, Computational evaluation of effectiveness for intratumoral injection strategies in magnetic nanoparticle assisted thermotherapy, Int. J. Heat Mass Transfer 148 (2020) 119129.

[25] Q. Jiang, F. Ren, C. Wang, Z. Wang, G. Kefayati, S. Kenjeres, K. Vafai, Y. Liu, H. Tang, On the magnetic nanoparticle injection strategy for hyperthermia treatment, Int. J. Mech. Sci. 235 (2022) 107707.

[26] Y.-d. Tang, T. Jin, R.C. Flesch, Impact of different infusion rates on mass diffusion and treatment temperature field during magnetic hyperthermia, Int. J. Heat Mass Transfer 124 (2018) 639–645.

[27] H.H. Pennes, Analysis of tissue and arterial blood temperatures in the resting human forearm, J. Appl. Physiol. 1 (2) (1948) 93–122.

[28] M. Salloum, R. Ma, L. Zhu, Enhancement in treatment planning for magnetic nanoparticle hyperthermia: optimization of the heat absorption pattern, Int. J. Hyperth. 25 (4) (2009) 309–321.

[29] Y. Tang, H. Su, R.C. Flesch, T. Jin, An optimization method for magnetic hyperthermia considering Nelder-Mead algorithm, J. Magn. Magn. Mater. 545 (2022) 168730.

[30] P. Di Barba, F. Dughiero, E. Sieni, Synthesizing distributions of magnetic nanoparticles for clinical hyperthermia, IEEE Trans. Magn. 48 (2) (2012) 263–266.

[31] Y.-D. Tang, T. Jin, R.C. Flesch, H.-Y. Jiang, Simultaneous optimization of injection dose and location for magnetic hyperthermia using metaheuristic algorithms, IEEE Trans. Magn. 56 (1) (2019) 1–6.

[32] P. Di Barba, F. Dughiero, E. Sieni, Field synthesis for the optimal treatment planning in magnetic fluid hyperthermia, Arch. Electr. Eng. (2012) 57–67.

[33] W. Dewey, L. Hopwood, S. Sapareto, L. Gerweck, Cellular responses to combinations of hyperthermia and radiation, Radiology 123 (2) (1977) 463–474.

[34] M.A. Swartz, M.E. Fleury, Interstitial flow and its effects in soft tissues, Annu. Rev. Biomed. Eng. 9 (1) (2007) 229–256.

[35] Y.-d. Tang, T. Jin, R.C. Flesch, Effect of mass transfer and diffusion of nanofluid on the thermal ablation of malignant cells during magnetic hyperthermia, Appl. Math. Model. 83 (2020) 122–135.

[36] R. Rahpeima, C.-A. Lin, Numerical study of magnetic hyperthermia ablation of breast tumor on an anatomically realistic breast phantom, Plos One 17 (9) (2022) e0274801.

[37] M.W. Dewhirst, B. Viglianti, M. Lora-Michiels, M. Hanson, P. Hoopes, Basic principles of thermal dosimetry and thermal thresholds for tissue damage from hyperthermia, Int. J. Hyperth. 19 (3) (2003) 267–294.

[38] M. Mohammadpour, B. Firoozabadi, Numerical study of the effect of vascular bed on heat transfer during high intensity focused ultrasound (HIFU) ablation of the liver tumor, J. Therm. Biol. 86 (2019) 102431.

[39] K. Yue, S. Zheng, Y. Luo, X. Zhang, J. Tang, Determination of the 3D temperature distribution during ferromagnetic hyperthermia under the influence of blood flow, J. Therm. Biol. 36 (8) (2011) 498–506.

[40] H.A. Sormoli, A. Mojra, G. Heidarinejad, Microbubble-enhanced HIFU therapy for vascularized tumors using levovist contrast agent, Int. J. Mech. Sci. 257 (2023) 108569.

[41] C.L. Carter, C. Allen, D.E. Henson, Relation of tumor size, lymph node status, and survival in 24,740 breast cancer cases, Cancer 63 (1) (1989) 181–187.

[42] A. AlAmiri, K. Khanafer, K. Vafai, Fluid-structure interactions in a tissue during hyperthermia, Numer. Heat Transf. Part A: Appl. 66 (1) (2014) 1–16.

[43] J. Lang, B. Erdmann, M. Seebass, Impact of nonlinear heat transfer on temperature control in regional hyperthermia, IEEE Trans. Biomed. Eng. 46 (9) (1999) 1129–1138.

[44] I. Hilger, W.A. Kaiser, Iron oxide-based nanostructures for MRI and magnetic hyperthermia, Nanomedicine 7 (9) (2012) 1443–1459.

[45] H. Liu, J. Zhang, X. Chen, X.-S. Du, J.-L. Zhang, G. Liu, W.-G. Zhang, Application of iron oxide nanoparticles in glioma imaging and therapy: from bench to bedside, Nanoscale 8 (15) (2016) 7808–7826.

[46] H. Zhang, Lattice Boltzmann method for solving the bioheat equation, Phys. Med. Biol. 53 (3) (2008) N15.

[47] J. Buongiorno, Convective transport in nanofluids, J. Heat Transf. (2006).

[48] B. Ghasemi, S. Aminossadati, A. Raisi, Magnetic field effect on natural convection in a nanofluid-filled square enclosure, Int. J. Therm. Sci. 50 (9) (2011) 1748–1756.

[49] L.S. Sundar, M.K. Singh, A.C. Sousa, Investigation of thermal conductivity and viscosity of Fe3O4 nanofluid for heat transfer applications, Int. Commun. Heat Mass Transfer 44 (2013) 7–14.

[50] Q. Liu, Y.-L. He, Q. Li, W.-Q. Tao, A multiple-relaxation-time lattice Boltzmann model for convection heat transfer in porous media, Int. J. Heat Mass Transfer 73 (2014) 761–775.

[51] L. Roizin-Towle, J.P. Pirro, The response of human and rodent cells to hyperthermia, Int. J. Radiat. Oncol.* Biol.* Phys. 20 (4) (1991) 751–756.

[52] Y. Tang, R.C. Flesch, T. Jin, A method for increasing the homogeneity of the temperature distribution during magnetic fluid hyperthermia with a Fe-Cr-Nb-B alloy in the presence of blood vessels, J. Magn. Magn. Mater. 432 (2017) 330–335.

[53] S.A. Sapareto, W.C. Dewey, Thermal dose determination in cancer therapy, Int. J. Radiat. Oncol.* Biol.* Phys. 10 (6) (1984) 787–800.

[54] S. Kossatz, R. Ludwig, H. Dähring, V. Ettelt, G. Rimkus, M. Marciello, G. Salas, V. Patel, F.J. Teran, I. Hilger, High therapeutic efficiency of magnetic hyperthermia in xenograft models achieved with moderate temperature dosages in the tumor area, Pharm. Res. 31 (2014) 3274–3288.

[55] A. Hervault, N.T.K. Thanh, Magnetic nanoparticle-based therapeutic agents for thermo-chemotherapy treatment of cancer, Nanoscale 6 (20) (2014) 11553–11573.

[56] C. Gu, J. Zhang, W. Gao, J. Wang, K. Mou, X. Zhang, J. Qi, Advances and applications of hyperthermia in tumor therapy: Mechanisms, techniques, and clinical integration, Int. Commun. Heat Mass Transfer 164 (2025) 108895.

[57] O. Lemine, S. Algessair, N. Madkhali, B. Al-Najar, K. El-Boubbou, Assessing the heat generation and self-heating mechanism of superparamagnetic Fe3O4 nanoparticles for magnetic hyperthermia application: the effects of concentration, frequency, and magnetic field, Nanomaterials 13 (3) (2023) 453.

[58] M. Ahamed, H. A. Alhadlaq, J. Alam, M. Khan, D. Ali, S. Alarafi, Iron oxide nanoparticle-induced oxidative stress and genotoxicity in human skin epithelial and lung epithelial cell lines, Curr. Pharm. Des. 19 (37) (2013) 6681–6690.

[59] D. Karponis, M. Azzawi, A. Seifalian, An arsenal of magnetic nanoparticles; perspectives in the treatment of cancer, Nanomedicine 11 (16) (2016) 2215–2232.

[60] J. Kennedy, R. Eberhart, Particle swarm optimization, in: Proceedings of ICNN'95-International Conference on Neural Networks, vol. 4, IEEE, 1995, pp. 1942–1948.

[61] Y. Shi, R.C. Eberhart, Empirical study of particle swarm optimization, in: Proceedings of the 1999 Congress on Evolutionary Computation-CEC99 (Cat. No. 99TH8406), vol. 3, IEEE, 1999, pp. 1945–1950.

[62] T.-C. Shih, H.-L. Liu, A.T.-L. Horng, Cooling effect of thermally significant blood vessels in perfused tumor tissue during thermal therapy, Int. Commun. Heat Mass Transfer 33 (2) (2006) 135–141.

[63] B. Gheflati, N. Naghavi, Computational study of nanoparticle assisted hyperthermia in tumors embedded with large blood vessels, Int. J. Heat Mass Transfer 151 (2020) 119415.

[64] Y. Tang, R.C. Flesch, T. Jin, Numerical investigation of temperature field in magnetic hyperthermia considering mass transfer and diffusion in interstitial tissue, J. Phys. D: Appl. Phys. 51 (3) (2017) 035401.

[65] Q. Jiang, F. Ren, C. Wang, Z. Wang, G. Kefayati, S. Kenjeres, K. Vafai, Y. Liu, H. Tang, Simulation of magnetic hyperthermia cancer treatment near a blood vessel, 2023, arXiv preprint arXiv:2308.14130.

[66] K.-H. Nam, E. Yeom, H. Ha, S.-J. Lee, Velocity field measurements of valvular blood flow in a human superficial vein using high-frequency ultrasound speckle image velocimetry, Int. J. Cardiovasc. Imaging 28 (2012) 69–77.

[67] H. Huang, P.-Y. Chen, C.-C. Huang, 40-MHz high-frequency vector Doppler imaging for superficial venous valve flow estimation, Med. Phys. 47 (9) (2020) 4020–4031.

[68] C. Laroche, F. Wells, R. Coulden, S. Stewart, M. Goddard, E. Lowry, A. Price, D. Gilligan, Improving surgical resection rate in lung cancer, Thorax 53 (6) (1998) 445–449.

[69] G. Gooiker, V. Lemmens, M. Besselink, O. Busch, B. Bonsing, I.Q. Molenaar, R. Tollenaar, I. De Hingh, M. Wouters, Impact of centralization of pancreatic cancer surgery on resection rates and survival, J. Br. Surg. 101 (8) (2014) 1000–1005.

[70] A. Latenstein, T. Mackay, L. Van Der Geest, C. van Eijck, V. de Meijer, M. Stommel, P. Vissers, M. Besselink, I. de Hingh, D.P.C. Group, Effect of centralization and regionalization of pancreatic surgery on resection rates and survival, Br. J. Surg. 108 (7) (2021) 826–833.

[71] M. Salloum, R. Ma, L. Zhu, An in-vivo experimental study of temperature elevations in animal tissue during magnetic nanoparticle hyperthermia, Int. J. Hyperth. 24 (7) (2008) 589–601.

[72] Q. Liu, Y.-L. He, Multiple-relaxation-time lattice Boltzmann model for simulating double-diffusive convection in fluid-saturated porous media, Int. J. Heat Mass Transfer 127 (2018) 497–502.